The Astrophysical Journal, 635:35–59, 2005 December 10

IDENTIFYING LENSES WITH SMALL-SCALE STRUCTURE. II. FOLD LENSES

Charles R. Keeton,[1] B. Scott Gaudi,[2] and A. O. Petters[3,4]

Received 2005 March 18; accepted 2005 August 19

ABSTRACT

When the source in a four-image gravitational lens system lies sufficiently close to a "fold" caustic, two of the lensed images lie very close together. If the lens potential is smooth on the scale of the separation between the two close images, the difference between their fluxes should approximately vanish, $R_{\rm fold} \equiv (F_+ - F_-)/(F_+ + F_-) \approx 0$. (The subscript indicates the image parity.) Violations of this "fold relation" in observed lenses are thought to indicate the presence of structure on scales smaller than the separation between the close images. We present a detailed study of the fold relation in realistic smooth lenses, finding it to be more subtle and rich than was previously realized. The degree to which $R_{\rm fold}$ can differ from zero for smooth lenses depends not only on the distance of the source from the caustic, but also on its location *along* the caustic, and then on the angular structure of the lens potential (ellipticity, multipole modes, and external shear). Since the source position is unobservable, it is impossible to say from $R_{\rm fold}$ alone whether the flux ratios in an observed lens are anomalous or not. Instead, we must consider the full distribution of $R_{\rm fold}$ values that can be obtained from smooth lens potentials that reproduce the separation d_1 between the two close images and the distance d_2 to the next nearest image. (By reducing the image configuration to these two numbers, we limit our model dependence and obtain a generic analysis.) We show that the generic features of this distribution can be understood, which means that the fold relation provides a robust probe of small-scale structure in lens galaxies. We then compute the full distribution using Monte Carlo simulations of realistic smooth lenses. Comparing these predictions with the data, we find that five of the 12 known lenses with fold configurations have flux ratio anomalies: B0712+472, SDSS 0924+0219, PG 1115+080, B1555+375, and B1933+503. Combining this with our previous analysis revealing anomalies in three of the four known lenses with cusp configurations, we conclude that at least half (8/16) of all four-image lenses that admit generic, local analyses exhibit flux ratio anomalies. The fold and cusp relations do not reveal the nature of the implied small-scale structure, but do provide the formal foundation for substructure studies, and also indicate which lenses deserve further study. Although our focus is on close pairs of images, we show that the fold relation can be used—with great care—to analyze all image pairs in all 22 known four-image lenses and reveal lenses with some sort of interesting structure.

Subject headings: cosmology: theory — dark matter — galaxies: formation — gravitational lensing — large-scale structure of universe

1. INTRODUCTION

Once baffling, the flux ratios between the images in four-image gravitational lens systems have recently become a source of considerable excitement. During the 1990s, standard smooth lens models (using ellipsoidal lens galaxies, plus tidal shear from lens environments) successfully handled ever-improving data on the number and relative positions of lensed images, but consistently failed to fit the image fluxes. The first step toward solving this problem came when Mao & Schneider (1998) realized that small-scale structure in lens galaxies, which had previously been neglected, could easily explain the "anomalous" flux ratios. The excitement began in earnest when Metcalf & Madau (2001) and Chiba (2002) pointed out that the cold dark matter (CDM) paradigm might naturally explain the sort of substructure required to fit the fluxes. Soon after, Dalal & Kochanek (2002) introduced a method of analyzing lens data to measure the properties of substructure. They concluded that $2.0^{+5.0}_{-1.4}\%$ (at 90% confidence) of the mass in lens galaxies is contained in substructure, which seemed to agree with CDM predictions, and to reveal that the so-called missing satellites (Moore et al. 1999; Klypin et al. 1999) are in fact present but dark. Anomalous flux ratios had become a powerful test of CDM on small scales, and potentially a unique probe of the fundamental nature of dark matter.

Before carrying the conclusions too far, though, we must recall that there are many links in the chain of logic from observations of flux ratio anomalies to tests of CDM that need to be filled in. First, we must identify lenses with anomalous flux ratios. Second, we should list all the different types of small-scale structure[5] that might create flux ratio anomalies, and understand what observations or analyses could distinguish between them. Third, we must see whether present data do distinguish different types of small-scale structure. If so, we can then quantify the amount of small-scale structure present in real lens galaxies. By comparing the inferred nature and abundance of small-scale structure to theoretical predictions, we can test the CDM paradigm. Finally, if we can understand how the predictions depend on the assumption that dark matter is cold and collisionless, we may be able to use lensing to probe the fundamental properties of the dark matter particle.

Dalal & Kochanek (2002) were the first to construct a realization of the full chain of logic. Briefly, they identified anomalous

[1] Department of Physics and Astronomy, Rutgers University, 136 Frelinghuysen Road, Piscataway, NJ 08837; keeton@physics.rutgers.edu.
[2] Harvard-Smithsonian Center for Astrophysics, 60 Garden Street, Cambridge, MA 02138; sgaudi@cfa.harvard.edu.
[3] Departments of Mathematics and Physics, Duke University, Durham, NC 27708; petters@math.duke.edu.
[4] Bass Fellow.

[5] The term "substructure" seems to have come to represent the sort of small-scale structure predicted by CDM. The term "small-scale structure" encompasses more general sorts of structure such as multipole modes, isophote twists, and tidal streams, so it is our term of choice.

flux ratios as those that could not be fit with standard lens models. They focused on radio flux ratios in order to ignore microstructure associated with individual stars in lens galaxies, and assumed that the only important small-scale structure is dark matter clumps of the sort predicted by CDM. (They argued that other sorts of small-scale structure, such as globular clusters and dwarf galaxies, are much less abundant than the inferred number of CDM clumps.) They assumed that the amount of CDM substructure is a universal fraction of the total density, used the lens observations to place constraints on that fraction, and then compared their results with predictions from CDM simulations. Making the various assumptions was necessary to build the first connection between lens flux ratios and the nature of dark matter. However, questions have been raised about some of them, which prompt us to go back and reassess each link in the chain. This evaluation is essential if we want to claim lensing as a reliable probe of small-scale structure in the universe. Moreover, it is intrinsically interesting because it will lead us to a deeper understanding of diverse topics in both lensing and structure formation theory.

Let us first consider the CDM end of the chain. There has been a surge of interest in refining predictions about substructure. It now appears that the substructure mass fraction need not be universal, but may vary both within a given halo and from one halo to another (e.g., Chen et al. 2003; Zentner & Bullock 2003; Mao et al. 2004; Oguri & Lee 2004). Tidal forces might be able to destroy dark matter clumps at the small radii where lensed images typically appear, in which case CDM might predict *too little* substructure to explain observed flux ratio anomalies (Mao et al. 2004; Amara et al. 2004). If so, we should consider whether small halos projected along the line of sight can provide sufficient small-scale structure. The situation is unclear, as Chen et al. (2003) claim that the millilensing optical depth from the line of sight is fairly small, while Metcalf (2005a, 2005b) claims that interloping structures are sufficient to explain flux ratio anomalies. Another possibility is that revised analyses of lens data may lower the required amount of small-scale structure (see below). A third possibility, of course, is that lensing and CDM simply disagree about small-scale structure. In any case, the important point is that the CDM predictions are challenging and still somewhat uncertain, and more work needs to be done. Mastering the theory involves both technical issues (numerical resolution) and physical effects (dynamical friction, tidal disruption), so it is not only essential for interpreting the lensing results, but also interesting in its own right.

Now moving to the lensing side, we must first ask whether flux ratio anomalies are real. Evans & Witt (2003) recently suggested that at least some of the "anomalies" might just be artifacts of certain assumptions in standard lens models. Specifically, instead of assuming the usual elliptical symmetry, they allowed perturbations from $m = 3$ and $m = 4$ multipole modes. Such modes are not only observed in the luminosity distributions of real galaxies (Bender et al. 1989; Saglia et al. 1993; Rest et al. 2001), but also predicted in the mass distributions of simulated galaxies (Heyl et al. 1994; Naab & Burkert 2003), so it does not seem unreasonable to allow them in lens models. Evans & Witt found that they could fit two of the three "anomalous" lenses they considered, without substructure. However, Congdon & Keeton (2005) found that multipole models fail to explain the strongest anomalies. Also, Kochanek & Dalal (2004) argued that even low-order multipole modes cannot explain an important statistical property of the ensemble of flux ratio anomalies: an asymmetry between images that form at minima of the time delay surface and those that form at saddle points, such that anomalous minima are almost always brighter than expected, while anomalous saddles are usually fainter than expected. To its credit, the CDM substructure hypothesis, and stellar microlensing, can both explain such an asymmetry (Metcalf & Madau 2001; Schechter & Wambsganss 2002; Keeton 2003; Bradač et al. 2004). However, it is not yet known whether alternative hypotheses could explain the asymmetry as well. In a different response to Evans & Witt, Yoo et al. (2005) recently showed that in PG 1115+080 the Einstein ring image of the quasar host galaxy rules out the sorts of multipole modes that would be needed to fit the quasar flux ratios. This type of analysis is very promising, but it demands deep, high-resolution, near-infrared observations combined with a sophisticated modeling analysis, and it must be applied on a case-by-case basis.

Clearly, a top priority must be to develop methods to determine whether flux ratio anomalies are real and indicate small-scale structure. One approach is to look for new data that cleanly reveal small-scale structure. The most unambiguous situation is the detection of flux perturbations associated with microlensing by stars in the lens galaxy. Detecting time variability in optical fluxes can prove that microlensing occurs (e.g., Woźniak et al. 2000; Schechter et al. 2003). Barring that, the next best thing is to take optical spectra of lensed images and use similarities or differences between emission line and continuum flux ratios to distinguish between microlensing, millilensing (a term sometimes applied to flux perturbations caused by CDM-type substructure), and errors in the macromodel (Moustakas & Metcalf 2003). The required observations are challenging, but the method does appear to be successful (Wisotzki et al. 2003; Metcalf et al. 2004; Morgan et al. 2004; Wayth et al. 2005a; Keeton et al. 2005). At this point, it is appropriate to note that the "more data" program has made it possible to conclude that, whatever their lensing interpretation may be, flux ratio anomalies are not electromagnetic phenomena. Measurements of flux ratios at different epochs and wavelengths have shown that differential extinction and scattering cannot explain the unusual observed flux ratios (see Koopmans et al. 2003a; Kochanek & Dalal 2004; Chiba et al. 2005; Appendix B).

An alternate approach is to reanalyze existing data. Traditionally, flux ratio anomalies have been identified as those that cannot be fit with certain smooth lens models (e.g., Dalal & Kochanek 2002; Metcalf & Zhao 2002; Kochanek & Dalal 2004). That analysis is, of course, susceptible to the criticism of being model-dependent. Perhaps even more important, it may be sensitive to certain global symmetries in the popular lens models that lead to global relations among the magnifications of the four images (Dalal 1998; Witt & Mao 2000; Hunter & Evans 2001; Evans & Hunter 2002). Failure to fit observed flux ratios may simply indicate failure of the global symmetries—which is very different from saying that there must be small-scale structure. To circumvent both of these problems, we would like to develop an analysis that is both *local* in the sense that it only depends on properties of the lens potential around and between closely spaced images, and *generic* in the sense that it does not depend on any specific properties of the types of models that are used to analyze the data.

Fortunately, lens theory has uncovered precisely what we need: local and generic relations between the magnifications between certain images in certain configurations. Specifically, two images in a "fold pair" (defined in § 2) should have magnifications μ_A and μ_B that satisfy the approximation relation $|\mu_A| - |\mu_B| \approx 0$, while three images in a "cusp triplet" should have

$|\mu_A| - |\mu_B| + |\mu_C| \approx 0$. This cusp relation played a central role in the analysis by Mao & Schneider (1998) that led to the idea that lens flux ratios may probe small-scale structure. If we want to use the fold and cusp relations today, however, we must rigorously understand how "local" and "generic" they really are, and whether they can actually be used as the basis of a realistic but robust method for identifying flux ratio anomalies that indicate small-scale structure.

The standard fold and cusp relations are derived from low-order Taylor series expansions in the vicinity of a fold or cusp caustic (Blandford & Narayan 1986; Mao 1992; Schneider & Weiss 1992; Schneider et al. 1992; Petters et al. 2001; Gaudi & Petters 2002a, 2002b). Formally, they are only valid when the source lies asymptotically close to a caustic. We have undertaken to reexamine the relations in more realistic settings, when the source sits a small but finite distance from a caustic, and the lens potential has a variety of nontrivial but smooth structures such as different radial profiles, ellipticities, octopole ($m = 4$) modes, and external tidal shears. In Keeton et al. (2003, hereafter Paper I), we studied the cusp relation. We found it to be insensitive to the radial profile of the lens galaxy, but quite sensitive to ellipticity, multipole modes, and shear. We quantified the degree to which these features can cause $|\mu_A| - |\mu_B| + |\mu_C|$ to deviate from zero even for smooth lenses. We then compared those allowed deviations with observed data and found that five observed lenses violate the realistic cusp relation in ways that indicate the presence of small-scale structure (B0712+472, RX J0911+0551, SDSS 0924+0219, RX J1131−1231, and B2045+265). We were very careful to state the limitations of the analysis, in particular to remark that study of the cusp relation—like all other analyses of single-epoch, single-band flux ratios—cannot reveal the nature of the implied small-scale structure. The strongest conclusion that can be drawn from a generic analysis is that the lens must have significant structure on scales smaller than the separation between the triplet of cusp images. We believe that this sort of deep discussion of the general features and applicability of a generic magnification relation is as valuable as the specific identification of flux ratio anomalies that it allows.

In this paper we turn our attention to the fold relation. We again seek to understand the general properties of the relation in realistic situations and to use that understanding to identify violations of the fold relation. We adopt the same basic approach as in Paper I: we first examine simple lens potentials analytically, then develop a Monte Carlo approach to study the fold relation in a realistic lens population, and finally use the realistic fold relation to look for flux ratio anomalies in observed lenses. However, many fine points of the discussion are rather different, because there are subtle but important ways in which the fold and cusp relations behave differently. In addition, we have come to understand that the fold relation may be used—with great care—to learn something interesting about image pairs that are not obviously fold pairs. The discussion of observed lenses therefore has a somewhat larger scope in this paper than it did in Paper I. One final difference is that the sample of published four-image lenses has grown by three since Paper I.

As in Paper I, we assert that, even though we adopt specific families of lens potentials, our analysis is more general than explicit modeling. One reason is that we take pains to understand what is generic in the fold relation. A second reason is that we have a better distinction between global and local properties of the lens potential. For example, a global $m = 1$ mode (i.e., a lack of reflection symmetry) would affect conclusions about anomalies in direct modeling, but not in our analysis. A third point is that our results are less *modeling*-dependent, less subject to the intricacies of fitting data and using optimization routines. A fourth advantage of our analysis is that, rather than simply showing that the standard models fail to fit a lens, it clearly diagnoses why. We believe that these benefits go a long way toward establishing that small-scale structure in lens galaxies is real and can be understood.

We must address a question that is semantic but important: Where do we draw the line between a normal "smooth" lens potential and "small-scale structure"? As in Paper I, we take a pragmatic approach and consider "smooth" lenses to include anything that is known to be common in galaxies, especially early-type galaxies: certain radial density profiles, reasonable ellipticities, small octopole modes representing disky or boxy isophotes, and moderate tidal shears from lens environments. Finding evidence for any or all of those in any given lens would not cause much stir. We then consider "small-scale structure" to be anything whose presence in lens galaxies would be notable and worthy of further study. In other words, we do not attempt to distinguish between microlensing, CDM-type substructure, massive and offset disk components, large-amplitude or intermediate-scale multipole modes, and so on, as explanations for flux ratio anomalies. That is properly the subject of a separate analysis, which can begin only once flux ratio anomalies have been rigorously identified.

The organization of the paper is as follows. In § 2 we introduce a way to quantify four-image lens configurations that is convenient for the fold relation. In § 3 we review the ideal magnification relations for folds and cusps. In § 4 we use a simple lens potential to examine the general properties of the fold relation in different regimes. In § 5 we introduce a Monte Carlo technique for characterizing the fold relation for a realistic population of lens potentials. In § 6 we use our understanding of the fold relation to evaluate all of the observed four-image lenses. We offer our conclusions and discussion in § 7. Two appendices provide supporting technical material. In Appendix A we present an important extension of the usual Taylor series analysis leading to the fold relation. In Appendix B we summarize the data that we analyze for all of the published four-image lenses.

2. CHARACTERIZING FOUR-IMAGE LENSES

At least 23 quadruply imaged lens systems are known. This count includes the 10 image system B1933+503, which is complex because there are two different sources that are quadruply imaged and a third that is doubly imaged (Sykes et al. 1998). It excludes PMN J0134−0931 and B1359+154 because each system has multiple lens galaxies that lead to image multiplicities larger than four (Rusin et al. 2001; Keeton & Winn 2003; Winn et al. 2003). The count also excludes systems like Q0957+561 in which some faint secondary features, including the host galaxy of the source quasar, may be quadruply imaged but are difficult to study (Bernstein et al. 1997; Keeton et al. 2000). Published data for the quadruply imaged systems are reviewed in Appendix B.

The image configurations of quad lenses can usually be classified "by eye" into three categories: folds, cusps,[6] and crosses. The names are related to the location of the source with respect to the lensing caustics. For our purposes it is more important to find a simple but quantitative way to characterize the configurations.

[6] Some authors subdivide cusps depending on whether they are associated with the long or short axis of the lens potential (e.g., Saha & Williams 2003), and we will follow suit when convenient.

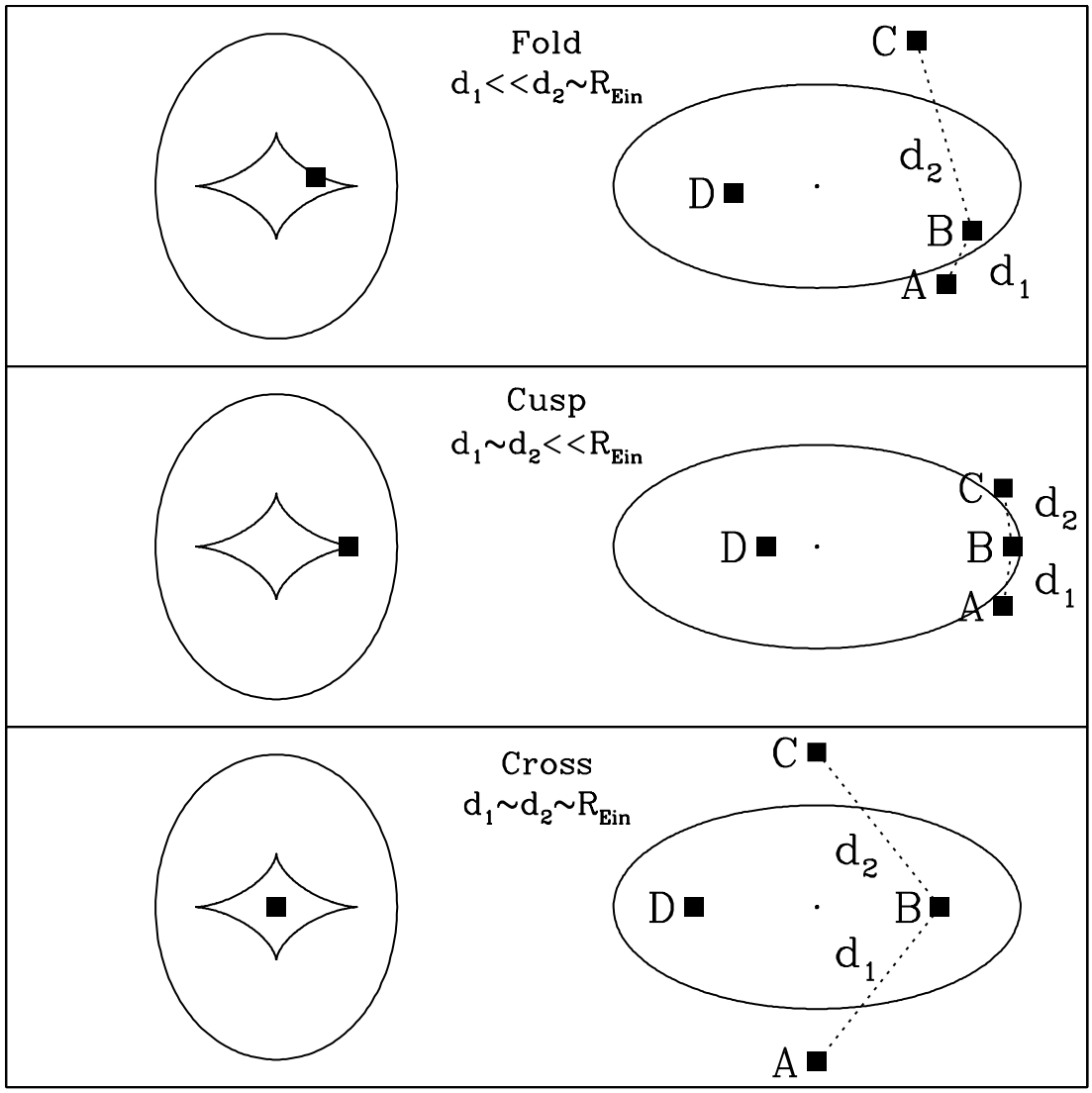

FIG. 1.—Three fiducial configurations of four-image lenses: fold (*top*), cusp (*middle*), and cross (*bottom*). In each panel the figure on the left shows the caustics and source position in the source plane, while the figure on the right shows the critical curves and image positions in the image plane. Despite appearances, the fold and cusp sources sit a finite distance from the caustic. The configurations are distinguished by the distances d_1 and d_2, as indicated.

When studying cusp lenses in Paper I, we used the separation and opening angle of a triplet of images. To study fold configurations, we are interested in pairs of images, in particular pairs comprising one image at a minimum of the time delay surface and one at a saddle point. (The parities of the images can usually be determined unambiguously; see Saha & Williams 2003.) Let us label the two minima M_1 and M_2, and the two saddles S_1 and S_2. (For definiteness, suppose M_1 is the brighter minimum and M_2 the fainter, and likewise for the saddles.) When considering the pair M_1S_1, for example, we define $d_1 = D(M_1, S_1)$ and $d_2 = \min[D(M_1, S_2), D(M_2, S_1)]$, where $D(i, j)$ is the distance between images i and j. In other words, d_1 is the separation between the images for the pair in question, and d_2 is the distance to the next nearest image. Note that d_1 and d_2 describe a *pair* of images. At times it is convenient to characterize the full configuration of all four images, and we define d_1^* and d_2^* to be the values of d_1 and d_2 for the pair with the smallest separation. In other words, a given four-image lens is fully characterized by the four values of (d_1, d_2) for the four different minimum/saddle pairs; but it is sometimes convenient to use (d_1^*, d_2^*) as an abbreviation that encodes the overall morphology of the lens.

Figure 1 illustrates the three fiducial configurations and indicates d_1 and d_2 for sample image pairs. In a fold lens, the source sits near a fold caustic, so two of the images lie close together with $d_1 \ll d_2$. Furthermore, d_2 is comparable to the other scale in the problem, the Einstein radius $R_{\rm Ein}$. In a cusp lens, the source is near a cusp caustic, so three of the images are close together and we have $d_1 \sim d_2 \ll R_{\rm Ein}$. If the source does not lie near a caustic, then the images form a relatively symmetric cross configuration with $d_1 \sim d_2 \sim R_{\rm Ein}$.

Incidentally, the three "archetypal" image configurations shown in Figure 1 were created using a singular isothermal ellipsoid lens with axis ratio $q = 0.5$ or ellipticity $e = 1 - q = 0.5$. We chose source positions such that $d_1^{\rm fold} = d_1^{\rm cusp} = d_2^{\rm cusp} = 0.46R_{\rm Ein}$, which is similar to the separation between close image pairs and triplets in observed fold and cusp lenses. The values $d_1^{\rm cross} = d_2^{\rm cross} = 1.54R_{\rm Ein}$ were set by the choice of ellipticity. We then chose the fold source position such that $d_2^{\rm fold} = d_1^{\rm cross} = d_2^{\rm cross}$. Having different distances be equal to each other means that we can smoothly morph from the fold to the cusp by fixing d_1 and varying d_2, or from the fold to the cross by fixing d_2 and varying d_1.

3. ASYMPTOTIC MAGNIFICATION RELATIONS FOR FOLDS AND CUSPS

In this section we briefly review the expected relations between the magnifications of images corresponding to a source near a fold or cusp caustic. The relations have been discussed before (Blandford & Narayan 1986; Mao 1992; Schneider & Weiss 1992; Schneider et al. 1992; Petters et al. 2001; Gaudi & Petters 2002a, 2002b), but we have extended the relations to a higher order of approximation.

As Paper I discussed in depth, when the source lies near a cusp caustic, the three associated images should have[7]

$$R_{\rm cusp} \equiv \frac{|\mu_{\rm A}| - |\mu_{\rm B}| + |\mu_{\rm C}|}{|\mu_{\rm A}| + |\mu_{\rm B}| + |\mu_{\rm C}|} = \frac{F_{\rm A} - F_{\rm B} + F_{\rm C}}{F_{\rm A} + F_{\rm B} + F_{\rm C}} \approx 0, \quad (1)$$

where μ_i is the signed magnification of image i, while $F_i = F_{\rm src}|\mu_i|$ is the flux of the image if the source has flux $F_{\rm src}$. ($R_{\rm cusp}$ is defined such that it is independent of $F_{\rm src}$.) In our naming convention, B is the middle of the three images and there is no need to specify whether it is a minimum or saddle image. To state equation (1) more precisely, we expand the lens mapping in a Taylor series about the cusp and find $R_{\rm cusp} = 0 + A_{\rm cusp} d^2 + \ldots$, where d is the maximum separation between the three images, while $A_{\rm cusp}$ depends on properties of the lens potential at the cusp point (physically, what matters is the ellipticity, higher order multipoles, and external shear; see Paper I). Since the constant and linear terms vanish, a source lying sufficiently close to the cusp produces three close images with $d \to 0$ and hence $R_{\rm cusp} \to 0$. As the source moves a small but finite distance from the cusp, the cusp relation picks up a correction term at second order in d. Nevertheless, for realistic distributions of ellipticity, multipole amplitudes, and shear, it is possible to derive reliable upper bounds on $R_{\rm cusp}$. Roughly speaking, we may say that those bounds can be violated only if the lens potential has significant structure on scales smaller than the distance between images, although Paper I provides a much more careful discussion.

Appendix A of this paper shows that when the source lies near a fold caustic, the two images near the fold critical point should have

$$R_{\rm fold} \equiv \frac{|\mu_{\rm min}| - |\mu_{\rm sad}|}{|\mu_{\rm min}| + |\mu_{\rm sad}|} = \frac{F_{\rm min} - F_{\rm sad}}{F_{\rm min} + F_{\rm sad}} \approx 0. \quad (2)$$

We are interested in pairs consisting of a minimum and a saddle, and we define $R_{\rm fold}$ such that the saddle image gets the minus sign in the numerator. Again, to be more precise we use a Taylor series expansion of the lens mapping near the fold point to find $R_{\rm fold} = 0 + A'(\Delta u)^{1/2} + \ldots$, where Δu is the perpendicular distance of the source from the caustic and A' is a constant that depends on local properties of the lens potential (see eq. [A19] in Appendix A). Working instead in the image plane, we can write $R_{\rm fold} = 0 + A_{\rm fold} d_1 + \ldots$, where d_1 is the distance between the two images (see eq. [A20]). The ideal fold relation $R_{\rm fold} \to 0$ holds only when the source is asymptotically close to the caustic. Now there is a correction term at first order in d_1, whose coefficient $A_{\rm fold}$ depends on properties of the lens potential (see eq. [A21]). In other words, the correction to the fold relation is of lower order than the correction to the cusp relation, which means that the fold relation is more sensitive to a small offset from the caustic. Thus, some care will be needed to determine whether an observed violation of the ideal fold relation really reveals small-scale structure or just indicates that the source lies a finite distance from a fold caustic.

[7] In Paper I we used the absolute value of $R_{\rm cusp}$, but it has become clear that the sign is an important component of theoretical predictions (e.g., Metcalf & Madau 2001; Schechter & Wambsganss 2002; Keeton 2003; Kochanek & Dalal 2004; Bradač et al. 2004), so we retain it now. Working with the signed quantity would not change the conclusions of Paper I.

4. UNDERSTANDING THE FOLD RELATION

4.1. *In the Asymptotic Regime*

We can begin to understand general features of the fold relation by examining the coefficient in the asymptotic limit for $R_{\rm fold}$,

$$A_{\rm fold} = \frac{3\psi_{122}^2 - 3\psi_{112}\psi_{222} + \psi_{2222}(1 - \psi_{11})}{6\psi_{222}(1 - \psi_{11})}, \quad (3)$$

where the ψ's represent various derivatives of the lens potential, evaluated at the fold point (see eqs. [A21]–[A23] in Appendix A). Imagine moving along the caustic and evaluating $A_{\rm fold}$ at various points. As we approach a cusp, $\psi_{222} \to 0$ while the other derivatives remain finite (e.g., Petters et al. 2001, p. 346), so $|A_{\rm fold}| \to \infty$. The sign depends on the type of cusp. A "positive" cusp has two minimum images and one saddle, and typically occurs on the long axis of the lens potential; it has $A_{\rm fold} \to -\infty$ with a minus sign because the saddle image is brighter than each minimum. A "negative" cusp has two saddles and one minimum, and typically occurs on the short axis of the potential; it has $A_{\rm fold} \to +\infty$ with a plus sign because the minimum image is brighter than each saddle. One implication of $|A_{\rm fold}| \to \infty$ is that the fold relation breaks down near a cusp, but that is not surprising because the asymptotic analysis in Appendix A explicitly assumes that we have chosen a fold point and are examining a small neighborhood that does not include a cusp point. Besides, near a cusp it is the cusp relation that ought to be satisfied, not the fold relation.

The more interesting implication is that $A_{\rm fold}$ can take on all real values, both positive and negative. Unless there is some remarkable discontinuity, there must be a region where $A_{\rm fold}$ changes sign. Figure 2 confirms that this is the case for a typical example, namely, an isothermal ellipsoid lens with axis ratio $q = 0.5$ or ellipticity $e = 1 - q = 0.5$. There is a region where $|A_{\rm fold}|$ is small or even zero, so that the ideal fold relation $R_{\rm fold} \to 0$ is quite a good approximation. In this region the distance d_2 is large,[8] but interestingly the smallest values of $|A_{\rm fold}|$ do not correspond to the largest values of d_2. Over the larger range where d_2 is large enough that the image configuration would be classified as a fold (roughly $d_2 \gtrsim 1$), we find $|A_{\rm fold}| \sim 0.1$–0.3. The important implication is that a lot of lenses that are clearly folds may nevertheless fail to satisfy the ideal fold relation $R_{\rm fold} \to 0$.

An even more important conclusion is that the validity of the ideal fold relation depends not just on whether the source is close to a fold caustic, but also on where the source is located *along* the caustic. This point is shown more directly in the next subsection.

4.2. *Across the Source Plane*

To move beyond the asymptotic regime, we use the software by Keeton (2001) to solve the lens equation exactly throughout

[8] The distance d_1 can be arbitrarily small depending on how close the source is placed to the caustic, but d_2 remains finite even when the source lies right on the caustic.

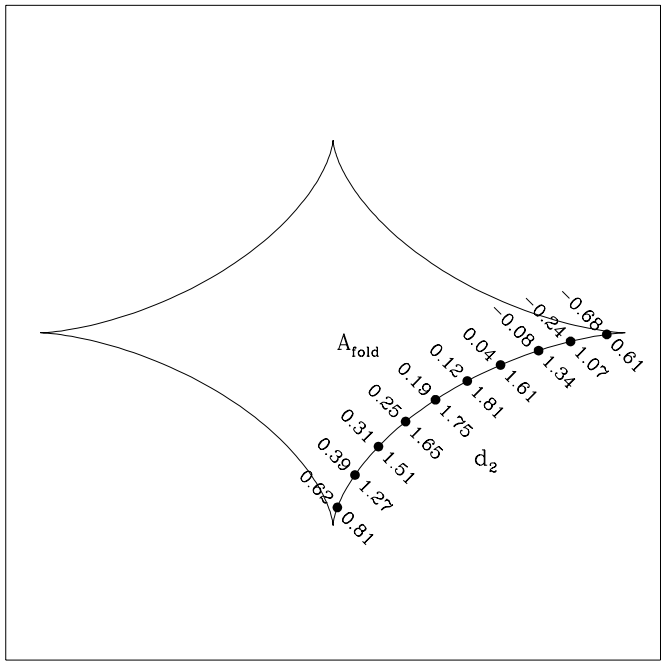

FIG. 2.—Caustic curve for an isothermal ellipsoid lens with an axis ratio $q = 0.5$, or ellipticity $e = 1 - q = 0.5$. The numbers above the points indicate values of the coefficient $A_{\rm fold}$ in the asymptotic fold relation $R_{\rm fold} = A_{\rm fold}\ d_1 + \ldots$ at various points along the caustic. (See eq. [A21] in Appendix A; recall that $A_{\rm fold}$ is to be evaluated *on* the caustic, but it then describes the fold relation in the *vicinity* of the caustic.) The numbers below the points indicate the corresponding values of d_2 (in units with $R_{\rm Ein} = 1$). The other quadrants can be filled in by symmetry.

the source plane for an isothermal ellipsoid lens with ellipticity $e = 0.5$. For each source inside the astroid caustic, we find the four images, identify the pair with the smallest separation, and then compute d_1, d_2, and $R_{\rm fold}$ for that pair. (These are by definition the same as d_1^* and d_2^*.) The results are shown in Figure 3. First, it is valuable to understand how d_1 and d_2 vary with source position, as shown in Figures 3*a* and 3*b*. The separation d_1 between the images measures very directly the distance of the source from the caustic. The distance d_2 to the next nearest image varies along the caustic and basically measures the distance of the source from a cusp. In general, fixing both d_1 and d_2 fixes the source to one of eight positions (two in each quadrant).

Figures 3*c* and 3*d* show $R_{\rm fold}$ as a function of source position, with contours of d_1 and d_2 overlaid. $R_{\rm fold}$ is large and negative near the long-axis cusp, and it is large and positive in a band extending from one short-axis cusp to the other and passing through the origin. The area in which $R_{\rm fold} > 0$ is larger than the area in which $R_{\rm fold} < 0$, which means that the distribution of $R_{\rm fold}$ values is not symmetric about $R_{\rm fold} = 0$. Near the origin, $R_{\rm fold}$ is large and positive. Both of these points will be important for our analysis of real lenses in § 6. There is a "wedge" of small $R_{\rm fold}$ values starting at the caustic but extending well inside; this corresponds to the region where the asymptotic coefficient $A_{\rm fold}$ is nearly zero (see Fig. 2). Interestingly, in the region near the caustic and midway between the cusps, where d_2 is large and where we would expect to find archetypal folds, $R_{\rm fold}$ is not terribly small. The source must get very close to the caustic before $R_{\rm fold}$ vanishes. A remarkable visual impression is that $R_{\rm fold}$ seems to be more correlated with the d_2 contours than with the d_1 contours.

Finally, by tabulating the results for all the different source positions we can plot $R_{\rm fold}$ in the (d_1, d_2) plane, as shown in Figures 3*e* and 3*f*.[9] There are two plots because there are two source positions in each quadrant, and hence two values of $R_{\rm fold}$, with the same values of d_1 and d_2. These figures show more clearly that $R_{\rm fold}$ vanishes as $d_1 \to 0$, but the speed with which that occurs depends on the value of d_2. Furthermore, in the upper left corner (the region of fold configurations), the $R_{\rm fold}$ contours bend over and become quite sensitive to d_2.

We are forced to conclude that the fold relation depends not only on proximity to a fold caustic, but also on location along the caustic. Although we are not shocked—we knew that the fold relation should break down near a cusp—we are nevertheless surprised to discover how sensitive $R_{\rm fold}$ is to location along the fold caustic even when the source is far from a cusp. This point is profound, because the location of the source along the caustic is not observable and cannot really be determined from the properties of the two images in the fold pair; it can only be inferred by considering the properties of the other two images as well. In particular, the distance d_2 to the next nearest image gives some indication of the location of the source along the caustic, and therefore plays a strong role in the fold relation.

We begin to suspect that using the fold relation in practice is not a simple matter of finding a close pair of images and asking how much they deviate from $R_{\rm fold} \approx 0$; the fold relation is in truth more subtle and rich.

4.3. *For All Four Image Pairs*

So far, among the four images in a given configuration we have only examined the pair with the smallest separation, because the fold relation best describes close pairs. The formalism can be applied to any pair, however, and to round out our general understanding of the fold relation it is instructive to examine all the pairs.

Figure 4 shows $R_{\rm fold}$ for all minimum/saddle image pairs, as a function of the distances d_1^* and d_2^* that characterize the image configuration. In the top panel we fix d_2^*, so varying d_1^* morphs the configurations from folds to crosses. The largest value of d_1^* corresponds to a symmetric cross, in which case the two minima are identical and the two saddles are identical, so all four minimum/saddle pairs have the same value of $R_{\rm fold}$. In the limit $d_1^* \to 0$ we obtain ideal folds, and the fold pair converges to $R_{\rm fold} \to 0$ (the ideal fold relation). In this limit two other pairs converge to $R_{\rm fold} \to \pm 1$, which is easily understood: the two fold images (A and B in Fig. 1) have much higher magnifications than the two other images, so the pairs AD and CB will both have $R_{\rm fold} \to \pm 1$. There is no intuitively obvious asymptotic limit for the pair of nonfold images (CD). The figure suggests that such limits do exist, but we suspect that they depend on properties of the lens potential in ways that the limits $R_{\rm fold} \to 0$ and ± 1 do not.

In the bottom panel we fix d_1^*, so varying d_2^* morphs the configurations between folds and cusps. Here the fold limit does not quite reach $R_{\rm fold} \to 0$ and ± 1 because we have fixed d_1^* to a finite value that does not actually correspond to an ideal fold. The more interesting limits are in the direction of cusps. As $d_2^* \to d_1^*$ we obtain a symmetric cusp configuration. For a symmetric ideal cusp, we can predict $R_{\rm fold} \to \pm\frac{1}{3}$ and ± 1 based on the following logic. By symmetry, $F_{\rm A} = F_{\rm C}$, so the ideal cusp relation implies $F_{\rm B} \approx 2F_{\rm A}$, and the fold relation then yields $R_{\rm fold} \approx \pm\frac{1}{3}$. The sign is positive (+) for a long-axis cusp (in which case B is a saddle), or negative (−) for a short-axis cusp (B is a minimum). At the same time, in an ideal cusp the images A, B, and C are all

[9] We generated the figures with Monte Carlo sampling of the source plane, which yields imperfect sampling of the (d_1, d_2) plane in the lower left corner.

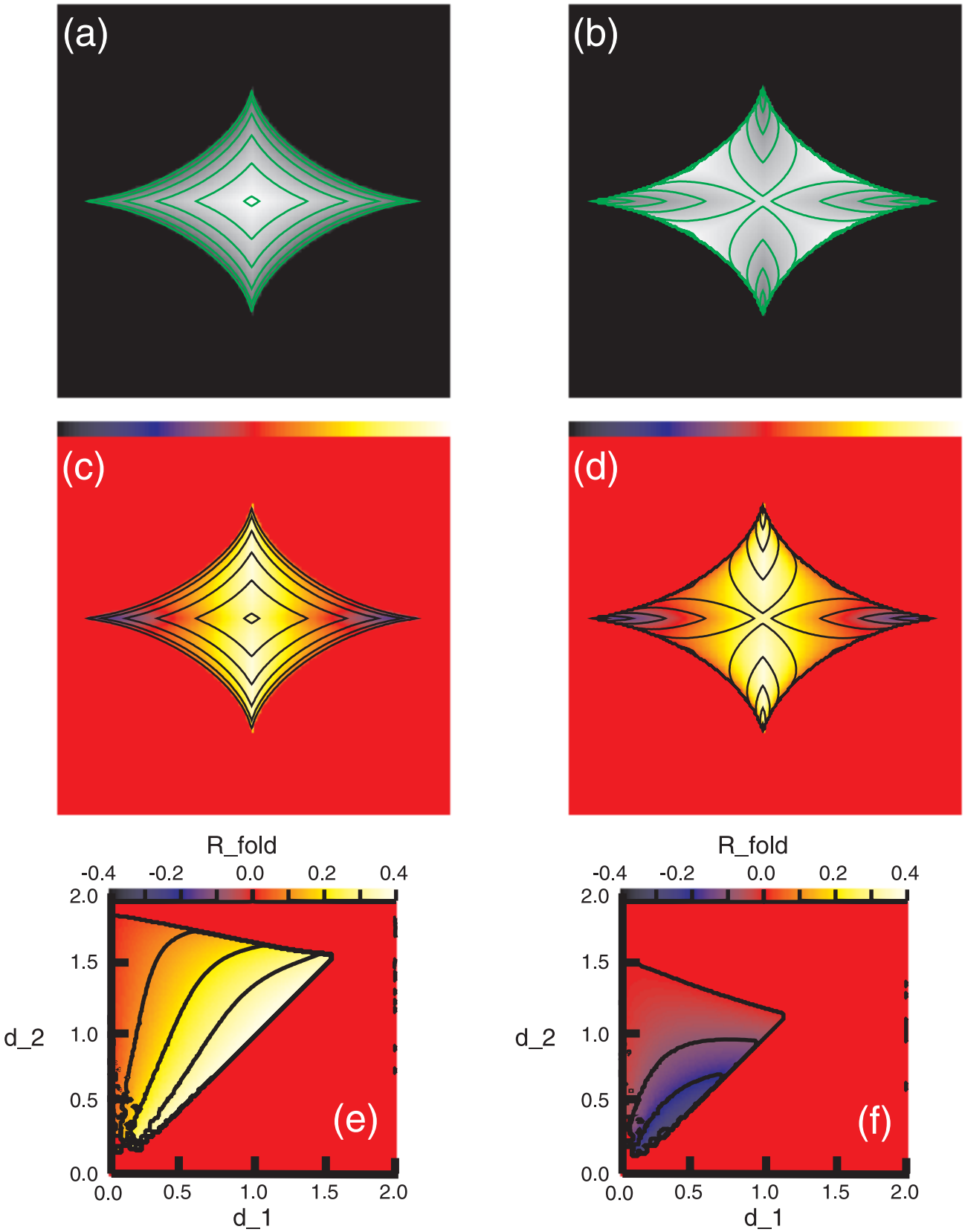

FIG. 3.—(*a*) Gray scale and contours both show the distance d_1 as a function of source position, for an isothermal ellipsoid lens with ellipticity $e = 0.5$. The contours range from 0 to 1.5 in steps of 0.25, in units with $R_{\rm Ein} = 1$. (*b*) The distance d_2 as a function of source position; the contours are again spaced by 0.25. (*c*) The colors show $R_{\rm fold}$ as a function of source position; the color coding is shown along the top edge of panel *e*. The d_1 contours from panel *a* are overlaid. (*d*) The colors again show $R_{\rm fold}$, with the d_2 contours from panel *b* now overlaid. (*e–f*) The colors and contours both show $R_{\rm fold}$ as a function of d_1 on the abscissa and d_2 on the ordinate; the contours range from -0.4 to 0.4 in steps of 0.1. Panel *e* shows the case $R_{\rm fold} > 0$, while panel *f* shows the case $R_{\rm fold} < 0$. Recall that folds have $d_1 \ll d_2 \sim R_{\rm Ein}$, cusps have $d_1 \sim d_2 \ll R_{\rm Ein}$, and crosses have $d_1 \sim d_2 \sim R_{\rm Ein}$. The region outside the triangles is inaccessible for this lens potential. Note that the figures were generated with Monte Carlo simulations and that the sampling is imperfect at $d_1 \sim d_2 \ll R_{\rm Ein}$.

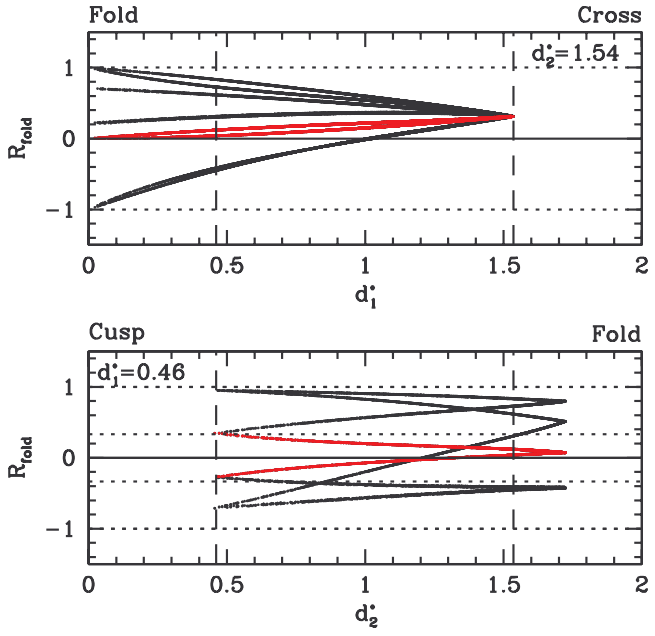

FIG. 4.—*Top:* $R_{\rm fold}$ as a function of the distance d_1^*, for fixed $d_2^* = 1.54$. Moving from left to right smoothly changes the image configuration from fold to cross. There are multiple curves because there are four image pairs for each image configuration, and there may be two different configurations with the same (d_1^*, d_2^*). For each configuration, the smallest separation pair is marked in red. *Bottom:* $R_{\rm fold}$ as a function of the distance d_2^*, for fixed $d_1^* = 0.46$. Moving from left to right smoothly changes the image configuration from cusp to fold. The horizontal lines show various asymptotic limits: $R_{\rm fold} \to 0$ for an ideal fold pair; $R_{\rm fold} \to \pm\frac{1}{3}$ for the two pairs of an ideal cusp triplet; and $R_{\rm fold} \to \pm 1$ for two other pairs in an ideal fold or cusp lens. The vertical lines indicate the separations for our archetypal lenses: $d_1^{*\rm fold} = d_1^{*\rm cusp} = d_2^{*\rm cusp} = 0.46$, and $d_2^{*\rm cusp} = d_1^{*\rm cross} = d_2^{*\rm cross} = 1.54$. We use an isothermal ellipsoid lens with ellipticity $e = 0.5$, and quote all lengths in units of $R_{\rm Ein}$.

much brighter than the fourth image D, so any pair involving D has $R_{\rm fold} \approx \pm 1$. As the source moves around the numerical values will change, but we generically expect two distinct values of $R_{\rm fold}$, one positive and one negative, for cusp lenses. Our archetypal cusp lens does not quite reach the asymptotic values because the source lies a finite distance from the cusp (d_1^* is 0.46 rather than $\approx$0), but it does confirm the basic reasoning.

Examining $R_{\rm fold}$ for widely separated image pairs in this way does not really tell us about small-scale structure, because we are no longer restricted to short length scales. Nevertheless, it is still helpful for obtaining a general understanding of the fold relation.

5. THE FOLD RELATION IN REALISTIC LENS POTENTIALS

While the ideal fold relation $R_{\rm fold} \to 0$ is completely general, it is only valid when the source is extremely close to a caustic. In realistic situations, the better approximation $R_{\rm fold} = A_{\rm fold} d_1$ depends on the source position and properties of the lens potential. In Paper I we explicitly showed that the properties of the lens potential affecting the cusp relation are ellipticity, low-order multipole modes, and tidal shear. Here we simply *define* a "realistic smooth lens" to be one that has these angular structures. (See § 1 for more discussion.) Unfortunately, the ellipticity, multipole moments, and shear in individual lenses cannot be observed directly. Ellipticity and multipole modes in the lens galaxy *light* may be measurable, but for lensing we need the properties of the *mass*. The mass properties could be constrained with lens modeling (with perhaps the best example being the analysis by Yoo et al. 2005), but we seek to avoid model dependence as much as possible. Instead, our approach is to adopt observationally motivated priors on the distribution of ellipticity, multipole modes, and shear and use Monte Carlo simulations to derive probability distributions for $R_{\rm fold}$ for a realistic lens population.

5.1. *Methods*

The simulation methods are the same as in Paper I, so we review the main points here and refer the reader to that paper for further details. We consider only isothermal radial profiles ($\Sigma \propto R^{-1}$) for the simulated galaxies, because in Paper I we showed that local analyses of the lens mapping are not very sensitive to changes in the radial profile. For the angular structure, we consider ellipticity, as well as additional octopole modes ($m = 4$ multipole perturbations). To model populations of early-type galaxies, we draw the ellipticities and octopole moments from measurements of isophote shapes in observed samples of early-type galaxies.[10] Even if the shapes of the light and mass distributions are not identical on a case-by-case basis, it seems reasonable to think that their distributions may be similar (see Rusin & Tegmark 2001). Indeed, the distribution of isodensity contour shapes in simulated merger remnants is very similar to the observed distribution of isophote shapes (Heyl et al. 1994; Naab & Burkert 2003). We use three different observational samples, because they have different strengths and weaknesses and allow a check for systematic effects:

1. Jørgensen et al. (1995) report ellipticities for 379 E/S0 galaxies in 11 clusters, including Coma. Their ellipticity distribution has mean $\bar{e} = 0.31$ and dispersion $\sigma_e = 0.18$. They do not report octopole moments.
2. Bender et al. (1989) report ellipticities and octopole moments for 87 nearby, bright elliptical galaxies. Their ellipticity distribution has mean $\bar{e} = 0.28$ and dispersion $\sigma_e = 0.15$, while their octopole moment distribution has mean $\bar{a}_4 = 0.003$ and dispersion $\sigma_{a_4} = 0.011$.
3. Saglia et al. (1993) report ellipticities and octopole moments for 54 ellipticals in Coma. Their ellipticity distribution has $\bar{e} = 0.30$ and $\sigma_e = 0.16$, while their octopole moment distribution has $\bar{a}_4 = 0.014$ and $\sigma_{a_4} = 0.015$.

The ellipticity and octopole distributions for the three samples are shown in Figure 6 of Paper I. All three samples are limited to low-redshift galaxies (by the need for good resolution to measure isophote shapes). We must assume that the distributions are reasonable for intermediate-redshift galaxies as well, which seems plausible if major mergers involving ellipticals are infrequent.

For the external shear amplitude, we adopt a lognormal distribution with median $\gamma = 0.05$ and dispersion $\sigma_\gamma = 0.2$ dex. This is consistent with the distribution of shears expected from the environments of early-type galaxies, as estimated from *N*-body and semianalytic simulations of galaxy formation by Holder & Schechter (2003). It is broadly consistent with the distribution of shears required to fit observed lenses. Dalal & Watson (2004) use a halo model calculation to suggest that the median shear should be more like $\gamma = 0.03$. However, the smaller median

[10] Most lenses are produced by early-type galaxies. Among the four-image lenses, the only known spiral lens galaxy is in Q2237+0305, and even there the images are most affected by the spheroidal bulge. This lens is not very important for our analysis, because it is a cross lens, and because it is already known to exhibit microlensing (e.g., Woźniak et al. 2000).

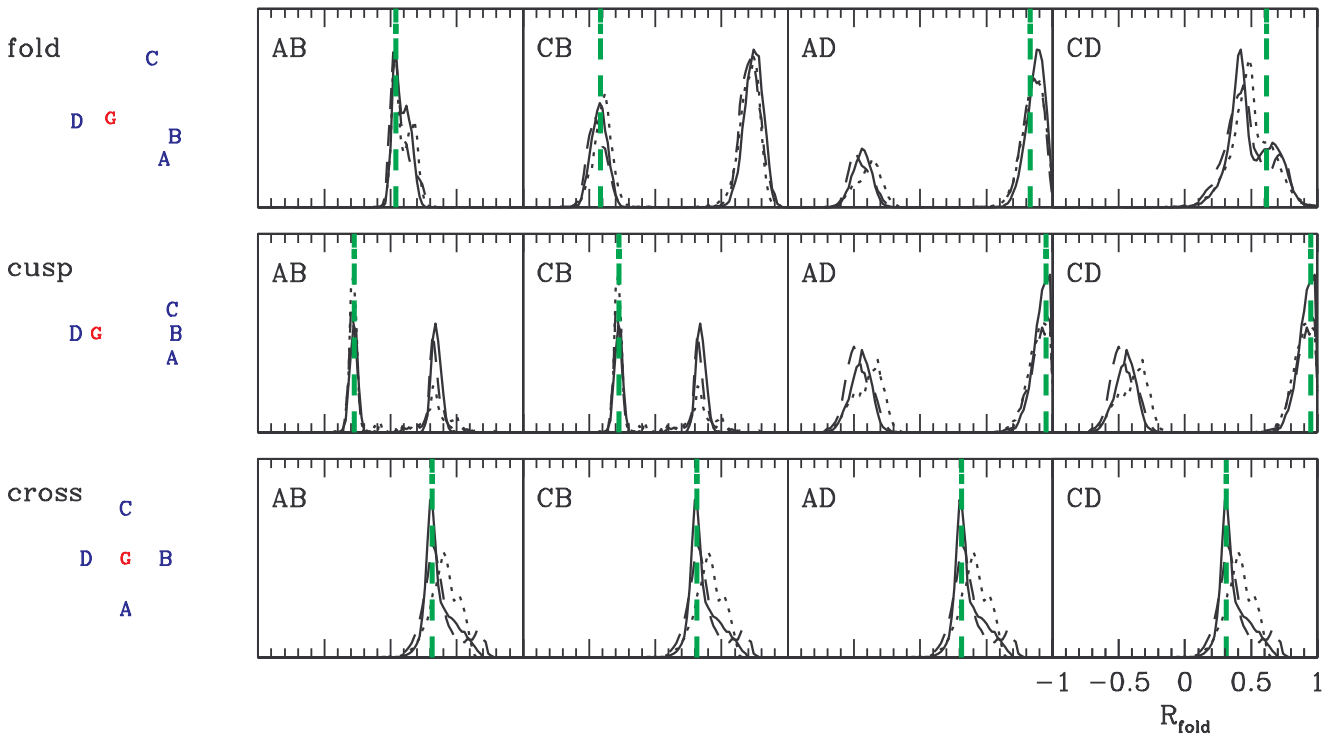

FIG. 5.—Probability distributions for $R_{\rm fold}$. On the left we show the image configurations, with lensed images (A–D) marked in blue and the lens galaxy (G) marked in red. The four columns then show $R_{\rm fold}$ for the different image pairs, sorted by increasing d_1 from left to right. (We adopt the convention of naming each pair such that the first letter indicates the minimum image while the second letter indicates the saddle.) The green vertical lines mark the actual values for our archetypal lenses. The black curves show the predicted distributions for realistic lens populations, with solid, dashed, and dotted curves showing results for Monte Carlo simulations based on the Jørgensen, Bender, or Saglia galaxy samples, respectively. The predicted distributions are normalized to unit area.

shear is not very compatible with the shears required to fit observed four-image lenses (e.g., Keeton et al. 1997). Furthermore, if we want to determine how much $R_{\rm fold}$ can deviate from zero for smooth lens potentials, then the conservative approach is to adopt the larger median shear. We assume random shear directions.

For each combination of ellipticity, octopole moment, and shear[11] we choose random sources with density $\sim 10^3 R_{\rm Ein}^{-2}$, solve the lens equation using the software by Keeton (2001), and compute $(d_1, d_2, R_{\rm fold})$ for each minimum/saddle image pair. For each input distribution, we examine a total of $\sim 10^6$ mock four-image lenses. Note that choosing sources with uniform density in the source plane has two important consequences. First, it ensures that each lens potential is automatically weighted by the correct lensing cross section. Second, it means that we neglect magnification bias, which would favor lenses with higher amplifications, and therefore give more weight to sources near the caustics that produce *small* deviations from the ideal fold relation. We therefore believe that neglecting magnification bias is the conservative approach when seeking to understand how large the deviations can be for smooth lens potentials.

5.2. *First Results*

We use our ensemble of mock image configurations to extract the probability distribution for $R_{\rm fold}$ at fixed values of d_1 and d_2.[12] Conceptually, this is like going to the appropriate point in the (d_1, d_2) plane of Figures 3*e* and 3*f* and reading off $R_{\rm fold}$, except that we now consider a large ensemble of lens potentials. To illustrate how we use these distributions, Figure 5 compares the value of $R_{\rm fold}$ for each image pair in our archetypal fold, cusp, and cross lenses to the appropriate conditional probability distribution $p(R_{\rm fold}|d_1, d_2)$ derived from the Monte Carlo simulations. If the observed value lies outside the predicted distribution, then we conclude that the image pair is inconsistent with lensing by a realistic population of smooth lens potentials. It is reassuring to see that our archetypal lenses (which were generated with a smooth lens) are indeed found to be consistent with lensing by a smooth potential.

We can observe some of the general features identified in § 4.3. Many of the distributions are bimodal, and some of those have two completely disjoint peaks. This is because given values of d_1 and d_2 can correspond to multiple source positions that yield different $R_{\rm fold}$ values (see Fig. 3). In the fold lens, the pair involving two fold images (AB) has $R_{\rm fold} \approx 0$. The two pairs involving one fold and one nonfold image (CB and AD) each have large $|R_{\rm fold}|$; they do not have $R_{\rm fold} \to \pm 1$ because the source sits a finite distance from the caustic, but the general trend that the fold pair has small $|R_{\rm fold}|$ while the two fold/nonfold pairs have large $|R_{\rm fold}|$ is confirmed. In the cusp lens, two pairs have $R_{\rm fold} \approx \pm\frac{1}{3}$ while the other two have large $|R_{\rm fold}|$. Again, the reason that the peaks in the AD and CD pairs do not actually reach $R_{\rm fold} \to \pm 1$ is because the source sits a finite distance from the caustic. Finally, in the cross case all four pairs have similar $R_{\rm fold}$ distributions—identical in the case of a symmetric cross—which are centered at some positive value but fairly broad. The consistency between our general analytic arguments and our detailed

[11] Note that we need not specify the galaxy mass, because for an isothermal lens the mass merely sets the length scale $R_{\rm Ein}$, and we can always work in units such that $R_{\rm Ein} = 1$.

[12] Strictly speaking, to accommodate our finite sampling of phase space, we consider all image configurations within ± 0.05 of the specified d_1 and d_2 values.

Monte Carlo simulations is reassuring and indicates that we have obtained new, deep insights into the fold relation.

6. APPLICATION TO OBSERVED LENSES

We are finally ready to examine the fold relation for observed four-image lenses. We summarize the data here (§ 6.1) and provide more details in Appendix B. Our main interest for the fold relation is of course fold image pairs (§ 6.2), but it is also interesting to consider the other image pairs in fold lenses (§ 6.3), as well as image pairs in cusp (§ 6.4) and cross (§ 6.5) lenses.

6.1. *Summary of the Data*

Table 1 lists the values of d_1, d_2, $R_{\rm Ein}$, and $R_{\rm fold}$ for all minimum/saddle image pairs in 22 known four-image lens systems,[13] and Appendix B provides some comments about the data. Most available flux ratio data come from broadband optical/near-infrared images or radio continuum observations. We consider separate optical and radio $R_{\rm fold}$ values, since they correspond to very different source sizes and therefore provide different information about small-scale structure. We also consider any other flux ratio data that are available: in the mid-infrared for Q2237+0305 (Agol et al. 2000) as well as PG 1115+080 and B1422+231 (Chiba et al. 2005), and the optical broad emission lines for HE 0435−1223 (Wisotzki et al. 2003), WFI 2033−4723 (Morgan et al. 2004), and SDSS 0924+0219 (Keeton et al. 2005).

We need the Einstein radius $R_{\rm Ein}$ to normalize d_1 and d_2. This must be determined from lens models, but it is quite robust and not very dependent on the choice of model (e.g., Kochanek 1991; Cohn et al. 2001). We treat the main lens galaxy as an isothermal ellipsoid with surface mass density

$$\kappa(r,\theta) = \frac{\Sigma(r,\theta)}{\Sigma_{\rm crit}} = \frac{R_{\rm Ein}}{2r[1-\epsilon\cos 2(\theta-\theta_\epsilon)]^{1/2}}, \qquad (4)$$

where $\Sigma_{\rm crit}$ is the critical surface density for lensing, ϵ is related to the axis ratio q of the galaxy by $\epsilon = (1-q^2)/(1+q^2)$, and θ_ϵ is the position angle of the galaxy. Few four-image lenses can be fit by a pure isothermal ellipsoid model, because elliptical lens galaxies tend not to be isolated. In most cases, modeling the environmental contribution to the lens potential as an external shear provides an excellent fit to the image positions (e.g., Keeton et al. 1997). The exceptions are HE 0230−2130, MG J0414+0534, RX J0911+0551, and B1608+656, each of which is known to have a satellite galaxy near the main lens galaxy that must be included in order to fit the image positions (Wisotzki et al. 1999; Schechter & Moore 1993; Koopmans et al. 2003b). We treat the satellite galaxies as isothermal spheres. We stress that when fitting the models to determine $R_{\rm Ein}$, we use only the relative positions of the images and the lens galaxy as constraints; it is not necessary to use the flux ratios as model constraints.

Figure 6 shows how the observed lenses populate the (d_1, d_2) plane. Although we have labeled them as folds, cusps, and crosses, in fact there is no sharp distinction between the fold and cross samples. SDSS 0924+0219 and B1933+503, which have $d_1/R_{\rm Ein} \sim 0.9$, could arguably be relabeled as crosses, although we choose not to do so (see § 6.2). The smooth transition simply reflects the fact that there are no sharp boundaries between different four-image configurations in the source plane.

In Figure 6 there is a particular region occupied by simulated lenses (*gray scale*), but it is specific to an isothermal ellipsoid lens with ellipticity $e = 0.5$. Varying the ellipticity and/or adding shear would move the upper edge so that the region could accommodate the other cross lenses. The two fold lenses at $d_2/R_{\rm Ein} \sim 2$ are a different story, though. These are HE 0230−2130 and B1608+656, each of which has two lens galaxies. Turning this around, we may say that observed lenses that are outliers in the (d_1, d_2) plane are likely to have complex lens potentials containing multiple galaxies.

[13] We do not analyze 0047−2808, as discussed in Appendix B.

6.2. *Fold Image Pairs*

We now examine the fold relation by comparing the observed $R_{\rm fold}$ values to the distributions expected for a realistic galaxy population. Figures 7 and 8 show the comparisons for the 12 fold lenses,[14] arranged in order of increasing $d_1^*/R_{\rm Ein}$. While there is a tremendous amount of information here, the discussion in § 4 helps us pick out the main trends. First, let us consider the various predicted distributions. When $d_1^*/R_{\rm Ein}$ is small, $R_{\rm fold}$ for the fold pair (the first column) is predicted to lie in a very narrow range near zero. This is the fold relation in its familiar form. At the same time, two other image pairs have distributions that feature two narrow and well-separated peaks (compare the top row of Fig. 5), while the fourth pair has a broad distribution with no particular center. As $d_1^*/R_{\rm Ein}$ increases, the distribution for the fold pair broadens while the two peaks for the next closest pair (the second column) tend to move closer together. HE 0230−2130 and B1608+656 buck these trends, for a simple reason: they have two lens galaxies, so they have configurations that are rare in our Monte Carlo simulations,[15] and that leads to narrow and unusual predicted $R_{\rm fold}$ distributions.

For most image pairs, there are no tremendous differences between the $R_{\rm fold}$ distributions from the three different simulations (based on the Jørgensen, Bender, or Saglia galaxy samples; also see Fig. 9). This gives us confidence that our conclusions are robust in the sense of not being very sensitive to the simulation input data.

Now we turn to the observed values of $R_{\rm fold}$. Many of them lie within the predicted range, so there is no obvious violation of the fold relation. The outliers are as follows:

1. *B0712+472*.—The optical data grossly violate the fold relation, but the radio data do not (as in the cusp relation; see Paper I). The wavelength dependence suggests that the optical anomaly is caused by microlensing.
2. *B1555+375*.—The radio data violate the fold relation at high confidence, as shown more clearly in Figure 9.
3. *PG 1115+080*.—The optical value of $R_{\rm fold}$ differs from the predictions at 99.2% confidence for the Jørgensen and Saglia simulations and at 96.1% confidence for the Bender simulations. The flux ratios can in principle be fit using large-amplitude multipole modes (Kochanek & Dalal 2004), but such modes are inconsistent with the Einstein ring image of the quasar host galaxy (Yoo et al. 2005). In other words, it appears that this lens is anomalous, but the model-independent evidence is not quite as secure as for the other anomalies. The mid-infrared value of $R_{\rm fold}$ differs from the optical value and agrees well with the predicted distribution, suggesting that the optical anomaly is created by microlensing.

[14] Note that we now include B0712+472 among the folds, even though we considered it a cusp in Paper I. Both classifications seem valid, depending on one's purpose. The close pair AB can be considered a fold, while the close triplet ABC can be considered a cusp. The source must lie close to the caustic in a region not far from a cusp. For the purposes of this paper, it is a fold.

[15] In fact, the Jørgensen and Saglia simulations do not contain *any* configurations with the same d_1 and d_2 values as the BD pair in B1608+656, to within the sampling resolution of our Monte Carlo simulations.

TABLE 1
LENS DATA

LENS	R_{Ein} (arcsec)	TYPE	IMAGE PAIR	d_1 (arcsec)	R_{fold} Optical	R_{fold} Radio	R_{fold} Other	REFERENCES
B0128+437	0.20	Fold	AB	0.14		0.263 ± 0.023		1
			AD	0.27		0.328 ± 0.028		
			CD	0.42		0.014 ± 0.042		
			CB	0.50		−0.058 ± 0.037		
HE 0230−2130	0.82	Fold	AB	0.74	0.000 ± 0.008			2
			CD	1.46				
			AD	1.64				
			CB	1.65	−0.289 ± 0.007			
MG 0414+0534	1.08	Fold	A_1A_2	0.41	−0.024 ± 0.038	0.085 ± 0.002		3, 4
			BA_2	1.71	−0.500 ± 0.043	−0.477 ± 0.004		
			A_1C	1.96	0.739 ± 0.015	0.736 ± 0.003		
			BC	2.13	0.400 ± 0.046	0.323 ± 0.007		
HE 0435−1223	1.18	Cross	CB	1.53	−0.029 ± 0.014		−0.035 ± 0.010	5, 6
			AB	1.59	0.226 ± 0.004		0.136 ± 0.005	
			CD	1.85	0.049 ± 0.019		0.137 ± 0.007	
			AD	1.88	0.299 ± 0.012		0.300 ± 0.011	
B0712+472	0.68	Fold/Cusp	AB	0.17	0.519 ± 0.052	0.085 ± 0.036		1, 7
			CB	0.91	−0.123 ± 0.075	−0.337 ± 0.051		
			CD	1.18	0.361 ± 0.062	0.672 ± 0.120		
			AD	1.25	0.636 ± 0.062	0.848 ± 0.060		
RX J0911+0551	0.95	Cusp	BA	0.48	0.027 ± 0.013			7
			BC	0.62	0.303 ± 0.012			
			DC	2.96	−0.137 ± 0.016			
			DA	3.08	−0.400 ± 0.014			
SDSS 0924+0219	0.87	Fold	AD	0.69	0.873 ± 0.002		0.821 ± 0.012	8
			AC	1.18	0.483 ± 0.003		0.696 ± 0.019	
			BD	1.46	0.751 ± 0.002		0.593 ± 0.023	
			BC	1.53	0.149 ± 0.002		0.363 ± 0.031	
SDSS 1004+4112	6.91	Fold	AB	3.73	0.194 ± 0.015			9, 10
			DB	11.44	−0.512 ± 0.017			
			AC	11.84	0.401 ± 0.011			
			DC	14.38	−0.312 ± 0.016			
PG 1115+080	1.03	Fold	A_1A_2	0.48	0.215 ± 0.011		0.036 ± 0.032	7, 11
			A_1B	1.67	0.722 ± 0.009		0.724 ± 0.104	
			CB	1.99	0.214 ± 0.019		0.135 ± 0.234	
			CA_2	2.16	−0.445 ± 0.011		−0.632 ± 0.060	
RX J1131−1231	1.81	Cusp	BA	1.19	0.209 ± 0.013			12
			CA	1.26	−0.272 ± 0.019			
			BD	3.14	0.824 ± 0.012			
			CD	3.18	0.587 ± 0.026			
HST 12531−2914	0.55	Cross	BC	0.77	−0.092 ± 0.057			7, 13
			AC	0.78	−0.187 ± 0.046			
			BD	0.91	0.164 ± 0.089			
			AD	1.02	0.015 ± 0.078			
HST 14113+5211	0.83	Cross	CD	1.13	0.138 ± 0.049			7, 14
			CB	1.38	0.287 ± 0.109			
			AD	1.41	0.128 ± 0.049			
			AB	1.42	0.305 ± 0.116			
H1413+117	0.56	Cross	AB	0.76	0.031 ± 0.016			3
			AC	0.87	0.205 ± 0.015			
			DC	0.91	−0.056 ± 0.023			
			DB	0.96	−0.229 ± 0.022			
HST 14176+5226	1.33	Cross	CB	1.73	0.088 ± 0.040			13
			AB	2.09	0.163 ± 0.040			
			CD	2.13	0.089 ± 0.043			
			AD	2.13	0.164 ± 0.040			
B1422+231	0.76	Cusp	AB	0.50	−0.038 ± 0.018	−0.038 ± 0.007	0.031 ± 0.027	3, 11, 15
			CB	0.82	−0.317 ± 0.020	−0.339 ± 0.006	−0.245 ± 0.055	
			AD	1.25	0.942 ± 0.019	0.936 ± 0.006		
			CD	1.29	0.898 ± 0.032	0.884 ± 0.011		

TABLE 1—*Continued*

Lens	R_{Ein} (arcsec)	Type	Image Pair	d_1 (arcsec)	R_{fold} Optical	R_{fold} Radio	R_{fold} Other	References
B1555+375	0.24	Fold	AB	0.09		0.274 ± 0.003		1, 16
			CB	0.35		−0.084 ± 0.004		
			AD	0.40		0.858 ± 0.006		
			CD	0.42		0.725 ± 0.010		
B1608+656	0.77	Fold	AC	0.87		0.321 ± 0.006		17
			BC	1.51		−0.016 ± 0.002		
			AD	1.69		0.706 ± 0.004		
			BD	2.00		0.486 ± 0.004		
B1933+503	0.49	Fold	4-3	0.46		0.656 ± 0.007		18, 19
			4-6	0.63		0.637 ± 0.007		
			1-3	0.90		0.143 ± 0.014		
			1-6	0.91		0.111 ± 0.013		
WFI 2026−4536	0.65	Fold	A_1A_2	0.33	0.181 ± 0.043			20
			A_1C	0.83	0.626 ± 0.015			
			BC	1.19	−0.431 ± 0.014			
			BA_2	1.28	0.096 ± 0.011			
WFI 2033−4723	1.06	Fold	A_1A_2	0.72	0.219 ± 0.010		0.174 ± 0.099	20
			A_1C	1.54	0.330 ± 0.007		0.056 ± 0.074	
			BA_2	2.01	−0.072 ± 0.012		−0.042 ± 0.091	
			BC	2.13	0.077 ± 0.044		−0.161 ± 0.057	
B2045+265	1.13	Cusp	AB	0.28	0.255 ± 0.017	0.287 ± 0.020		7, 21
			CB	0.56	0.153 ± 0.023	0.133 ± 0.045		
			AD	1.91		0.809 ± 0.022		
			CD	1.93		0.750 ± 0.033		
Q2237+0305	0.85	Cross	AD	1.01	Variable; see text	0.130 ± 0.145	−0.008 ± 0.068	22, 23, 24
			BD	1.18		0.172 ± 0.139	0.048 ± 0.062	
			AC	1.37		0.289 ± 0.170	0.270 ± 0.079	
			BC	1.40		0.328 ± 0.163	0.319 ± 0.072	

Notes.—The lengths R_{Ein} and d_1 are given in arcseconds. We do not explicitly quote d_2, because it can be determined from the other d_1 values. For example, in B0128+437 the value of d_2 for image pair AB would be the smaller of d_1(AD) and d_1(CB).

References.— (1) Koopmans et al. 2003a; (2) Wisotzki et al. 1999; (3) Falco et al. 1999; (4) Trotter et al. 2000; (5) Wisotzki et al. 2002; (6) Wisotzki et al. 2003; (7) Cfa-Arizona Space Telescope Lens Survey (CASTLES); (8) Keeton et al. 2005; (9) Oguri et al. 2004; (10) Inada et al. 2005; (11) Chiba et al. 2005; (12) Sluse et al. 2003; (13) Ratnatunga et al. 1995; (14) Fischer et al. 1998; (15) Patnaik et al. 1999; (16) Marlow et al. 1999; (17) Fassnacht et al. 2002; (18) Sykes et al. 1998; (19) Biggs et al. 2000; (20) Morgan et al. 2004; (21) Fassnacht et al. 1999; (22) Woźniak et al. 2000; (23) Falco et al. 1996; (24) Agol et al. 2000.

4. *SDSS 0924+0219*.—Although AD is not a particularly close pair (making the predicted R_{fold} distribution fairly broad), image D is so faint that there is a gross violation of the fold relation in both broadband and broad emission line flux ratios. Differences between the flux ratios plus time variability suggest the presence of microlensing (Kochanek 2005; Keeton et al. 2005).

5. *B1933+503*.—Although the 4/3 image pair is not particularly close, image 4 is so bright that there is a clear violation of the fold relation in the radio data.

HE 0230−2130 and B1608+656 deserve mention because each has two lens galaxies. In HE 0230−2130, the observed R_{fold} value shows images A and B to be more similar than expected for simple smooth lens potentials. In B1608+656, the observed R_{fold} value agrees with the predictions for simple lenses, which seems coincidental. These systems show that violations of the fold relation can reveal the lens potential to contain structure that is complex but not necessarily small-scale. That raises the question of whether any of the other anomalies could be caused by something large like a second galaxy. Probably not: in both of these systems the second galaxy was already known from direct observations and analyses of the image positions (see § 6.1). In other words, it is difficult for a massive second galaxy to escape notice. We therefore believe that the "second galaxy" hypothesis is not a valid explanation for most flux ratio anomalies.

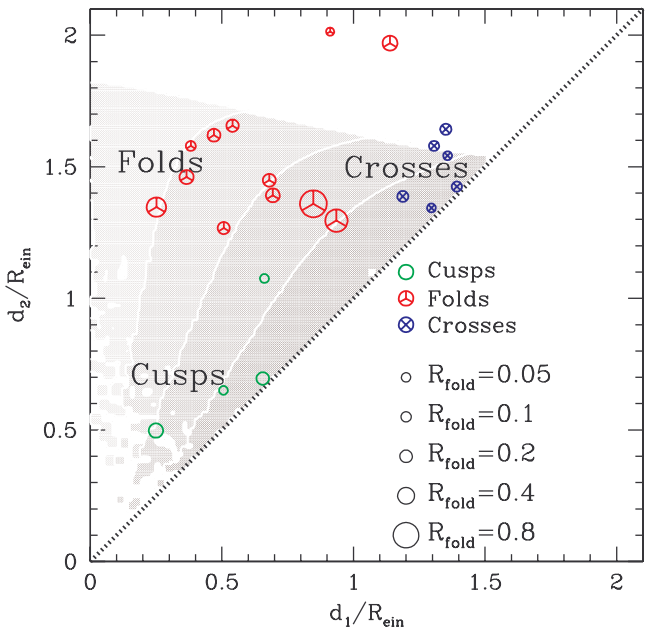

Fig. 6.—Colored points mark the locations of known four-image lenses in the plane of d_1/R_{Ein} and d_2/R_{Ein}. The color indicates the visual classification as a fold, cusp, or cross, while the point size indicates the value of R_{fold}. To help guide the eye, the gray scale shows R_{fold} for an isothermal ellipsoid lens with ellipticity $e = 0.5$ (from Fig. 3*e*).

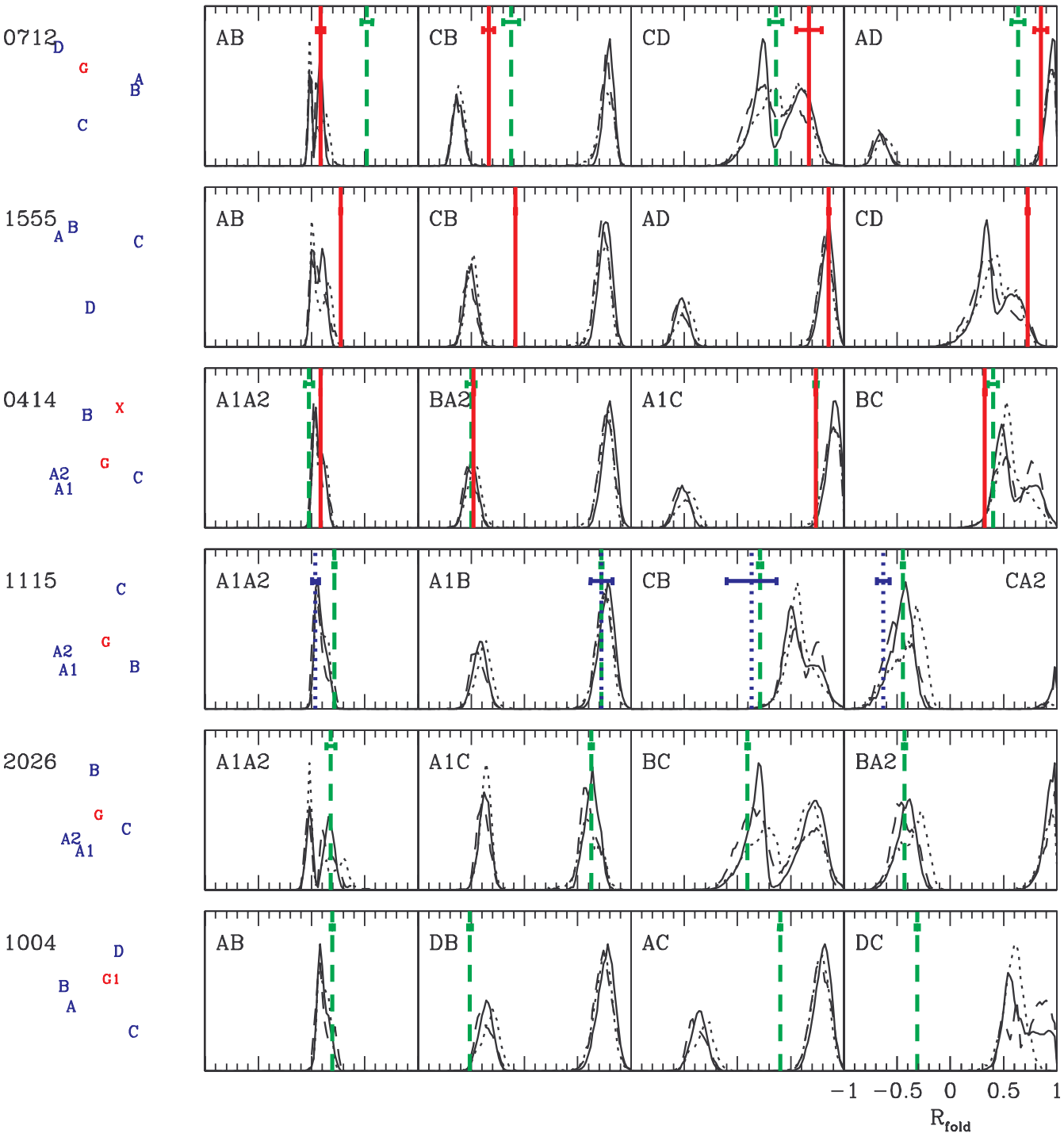

FIG. 7.—Observed and predicted $R_{\rm fold}$ values, for six of the known fold lenses. The black curves show the predicted distributions for realistic lens populations, as in Fig. 5. The vertical colored lines show the observed values and their uncertainties, with green indicating optical/near-infrared data and red indicating radio data. For PG 1115+080, the blue lines indicate mid-infrared data (Chiba et al. 2005). All data are listed in Table 1. The lenses are sorted by increasing $d_1^*/R_{\rm Ein}$ from top to bottom. For each lens, the image pairs are sorted by increasing $d_1/R_{\rm Ein}$ from left to right.

To summarize, our analysis of the fold relation reveals two flux ratio anomalies that were already known from violations of the cusp relation (B0712+472 [optical] and SDSS 0924+0219 [optical]). It also reveals strong new evidence for fold flux ratio anomalies in B1555+375 (radio) and B1933+503 (radio), plus good but slightly less strong evidence for a fold anomaly in PG 1115+080 (optical). In addition, a violation of the fold relation in HE 0230−2130 (optical) is presumably due to the presence of a second lens galaxy in that system.

While these specific conclusions are valuable, there are some important general lessons as well. First, even the closest observed fold image pairs have predicted $R_{\rm fold}$ distributions with a finite width. Therefore, a nonzero $R_{\rm fold}$ value in the range $R_{\rm fold} \sim 0$–0.2 *cannot* generally be taken to indicate a flux ratio anomaly. As a rule of thumb, when $d_1/R_{\rm Ein} \lesssim 0.4$ it does appear that a value $R_{\rm fold} \gtrsim 0.2$ is likely to indicate an anomaly, although we caution that this is just a rule of thumb and a full analysis of the predicted $R_{\rm fold}$ distribution must be done to reliably identify an anomaly.

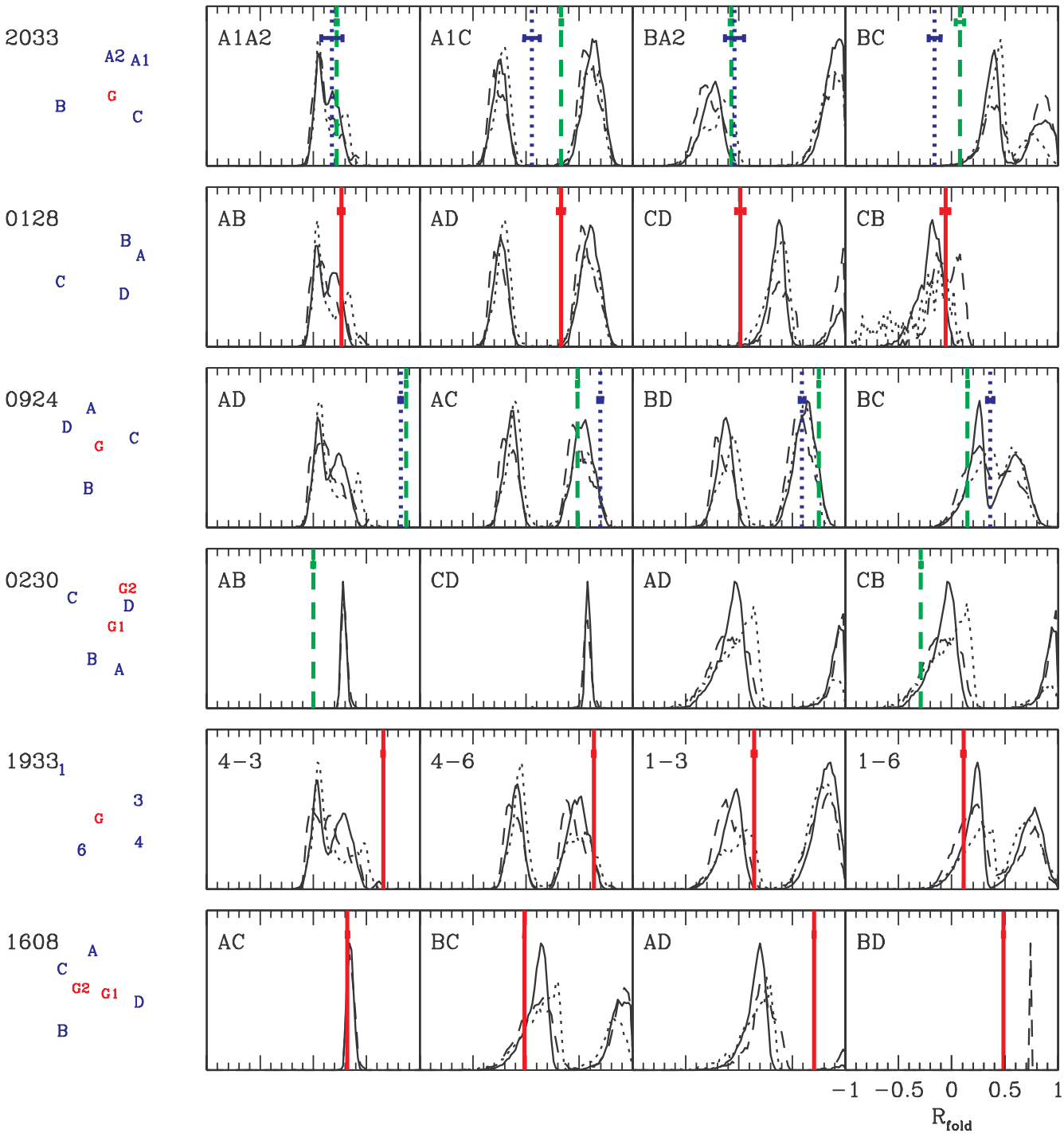

FIG. 8.—Similar to Fig. 7, but for the remaining six known fold lenses (again sorted by $d_1^*/R_{\rm Ein}$). For SDSS 0924+0219 and WFI 2033−4723, the vertical green lines show data from broadband optical flux ratios, while the vertical blue lines show data from optical emission-line flux ratios (Morgan et al. 2004; Keeton et al. 2005).

The importance of the full analysis becomes clear when we consider PG 1115+080, WFI 2026−4536, and SDSS 1004+4112. These three lenses have similar configurations with $d_1/R_{\rm Ein} \approx 0.5$, and (curiously enough) they all have $R_{\rm fold} \approx 0.2$. Yet one is anomalous (PG 1115+080), while the other two are fully compatible with the predicted distributions. What is more, the predicted distributions for WFI 2026−4536 are bimodal and qualitatively different from those for the other two lenses, even though all three image configurations are visually similar. These lenses teach the lesson that identifying fold flux ratio anomalies is not a simple matter of finding a close pair of images and asking whether $R_{\rm fold} \to 0$. The distance from $R_{\rm fold} \to 0$ that is needed to provide strong evidence for an anomaly depends in a complicated way on various properties of the lens potential that cannot be directly observed. Only a full and careful analysis of the fold relation can handle these issues.

We conclude that violations of the fold relation can be used to find flux ratio anomalies in a fairly model-independent way. However, that analysis is more subtle than was previously realized. It is necessary to know not only the separation d_1 between

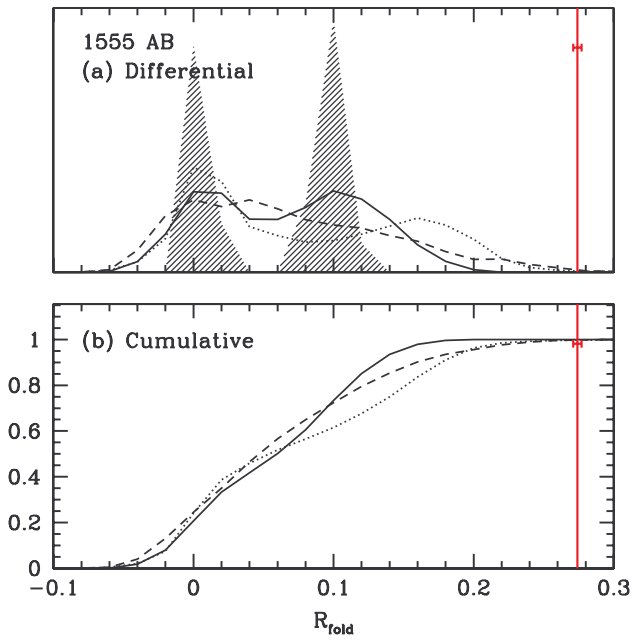

FIG. 9.—(*a*) Close-up of the AB panel for B1555+375 from Fig. 7. The red line shows the observed radio value for $R_{\rm fold}$, with its uncertainty (see Table 1). The solid, dashed, and dotted curves show the predicted $R_{\rm fold}$ distributions for Monte Carlo simulations based on the Jørgensen, Bender, and Saglia galaxy samples, respectively. For comparison, the hatched region shows the distributions for an isothermal ellipsoid with ellipticity $e = 0.5$. (*b*) Similar to panel *a*, but showing cumulative probability distributions.

the two images, but also the distance d_2 to the next nearest image, and to account for the finite width of the $R_{\rm fold}$ distribution expected for smooth lenses.

Finally, it is worthwhile to comment that all 12 of the fold image pairs have $R_{\rm fold}$ values that are positive or consistent with zero. An important prediction to emerge from theoretical studies is that small-scale structure (either dark matter clumps or stars) should tend to amplify minimum images and/or suppress saddle images (Metcalf & Madau 2001; Schechter & Wambsganss 2002; Keeton 2003; Bradač et al. 2004). Since either possibility would make $R_{\rm fold} > 0$, seeing only nonnegative values is certainly consistent with the substructure hypothesis (see Kochanek & Dalal 2004). It is inconsistent with nongravitational explanations of flux ratio anomalies (such as extinction or scattering), because those should affect minimum and saddle images in the same way. What is less clear is whether lumpy substructure is the only thing that can explain the asymmetry between minima and saddles, or whether small-scale but smooth structure is a viable alternative. Our analysis does offer an intriguing hint: nearly all the weight in our predicted $R_{\rm fold}$ distributions lies at $R_{\rm fold} > 0$, which indicates that even smooth, global features like ellipticity and shear affect minima and saddles differently. Still, it is not clear whether smooth features can explain the further asymmetry that all the anomalous $R_{\rm fold}$ values *exceed* the predictions. The minimum/saddle asymmetry appears to be a very promising probe of small-scale structure, but much more study is clearly called for.

6.3. *Other Image Pairs in Fold Lenses*

We can also consider the $R_{\rm fold}$ values for the other image pairs in fold lenses, although we must be careful about how we interpret them. As discussed in §§ 4.3 and 5.2, there are some useful general properties of the fold relation for these other image pairs. For example, the predicted $R_{\rm fold}$ distribution for a pair comprising a fold image and a nonfold image has two narrow peaks, one positive and one negative. While we are not aware of a simple way to predict the specific values, it seems from Figures 7 and 8 that they depend mainly on $d_1^*/R_{\rm Ein}$.

There are several image pairs for which the observed $R_{\rm fold}$ value lies far from the peaks in the predicted distributions: CB in B0712+472, CB in B1555+375, AC and DC in SDSS 1004+4112, and A_1C and BC in WFI 2033−4723.[16] The relatively large distance between the images in each pair prevents us from concluding that the discrepancies reveal "small-scale" structure in the lens. We can still conclude, though, that each pair is inconsistent with smooth lens models containing moderate ellipticities, octopole moments, and shears. Indeed, two of these lenses are already known to have complex potentials. SDSS 1004+4112 is produced by a cluster of galaxies (Oguri et al. 2004), while WFI 2033−4723 appears to lie in a group of galaxies with at least six perturbers lying within 20″ of the main lens galaxy (Morgan et al. 2004).

The situation seems different for the CB pair in PG 1115+080 and the CD pair in B0128+437. In these cases the observed values lie in the tail of the predicted distributions, at around the 1% probability level. It may be that having two "rare" values among 88 image pairs is statistically unsurprising, although it is hard to know how to quantify that possibility because the 88 pairs are not all independent. Alternatively, it may be that modest changes in the assumed distributions of ellipticity, octopole moment, and shear could raise the tail of the predicted $R_{\rm fold}$ distribution enough to make the observed values seem less unusual.

Overall, we conclude that gross discrepancies between observed and predicted $R_{\rm fold}$ values for the "other" pairs in fold lenses indicate complex structure in the lens potential. It is not necessarily small-scale structure, but it is still interesting and worth studying with detailed lens models.

6.4. *Cusp Lenses*

A cusp configuration has a close triplet of images that can be thought of as two close pairs. As discussed in §§ 4.3 and 5.2, we expect the predicted $R_{\rm fold}$ distribution for each pair to have two narrow and well-separated peaks. This constitutes a sort of "fold relation" for cusp lenses, which might help us better understand flux ratio anomalies in these systems.

Figure 10 compares the observed and predicted $R_{\rm fold}$ distributions for the four observed cusp lenses. Image pairs like BA in RX J0911+0551 and BA in RX J1131−1231, which have observed $R_{\rm fold}$ values lying between and far from the two predicted peaks, appear to indicate anomalies. In one sense these conclusions are not new, because these anomalies had already been identified through violations of the cusp relation (see Paper I). However, the fold relation can help us determine which of the three images is most anomalous. In RX J0911+0551, the violation of the fold relation is stronger in the BA pair than in the BC pair, so we infer that image A is probably the one most affected by small-scale structure. Similar reasoning leads to the conclusion that image B in RX J1131−1231 is the most anomalous. There could in fact be more than one perturbed image (see Dobler & Keeton 2005 for examples among other lenses), but the important point is that the fold relation can suggest which

[16] Note that in WFI 2033−4723 the differences between the optical continuum flux ratios and the emission-line flux ratios are interpreted as evidence for microlensing (see Morgan et al. 2004).

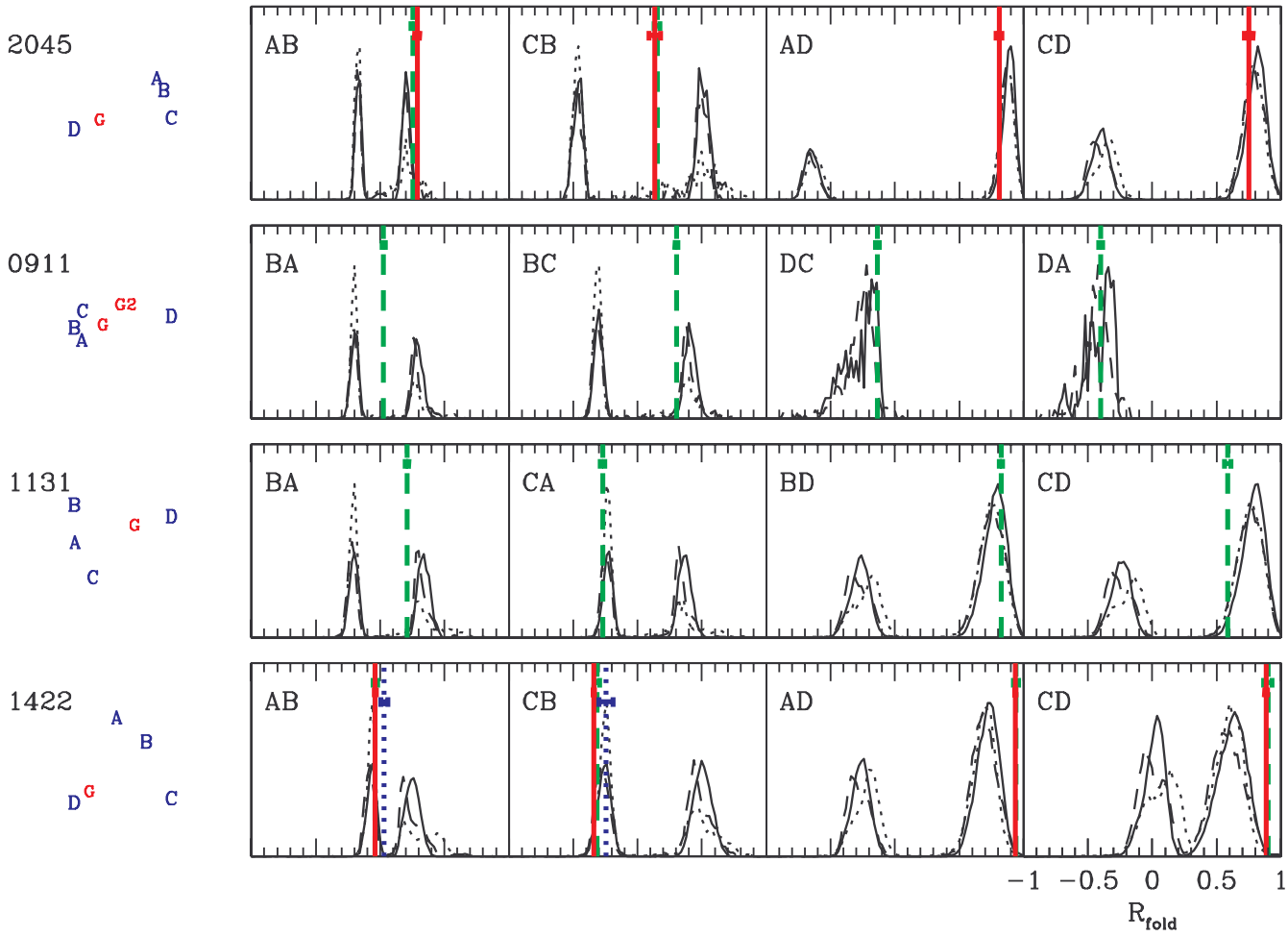

FIG. 10.—Similar to Fig. 7, but for the known cusp lenses. Again, the vertical green lines show optical/near-infrared values of $R_{\rm fold}$, while the vertical red lines show radio values. For B1422+231, the vertical blue lines show mid-infrared values of $R_{\rm fold}$ (Chiba et al. 2005).

image is most anomalous—a distinction that could not be made by the cusp relation.

The CB pair in B2045+265 illustrates a curious aspect of this analysis. For this lens, simulations without octopole modes (using the Jørgensen data) predict an $R_{\rm fold}$ distribution consisting of two narrow peaks far from the observed values. However, in simulations that include octopole modes (using the Bender or Saglia data), there is a small but finite probability for $R_{\rm fold}$ to lie between the two peaks. In this case, the possibility that octopole modes may be present limits our ability to declare that the fold relation is violated. This result is surprising because B2045+265 shows a very strong violation of the cusp relation, even when octopole modes are considered (see Paper I). The difference must be that the cusp relation considered three images simultaneously, while the fold relation considers them in two separate pairs.

Finally, we remark that the fold relation does not indicate anomalies among three cusp images in B1422+231. This is consistent with our conclusion from Paper I that generic magnification relations do not identify anomalies in this lens, even though detailed lens modeling suggests that it is indeed anomalous (Mao & Schneider 1998; Bradač et al. 2002; Metcalf & Zhao 2002; Dobler & Keeton 2005). Bradač et al. (2002, 2004) claim that the challenge for smooth lens models is not just the relative brightnesses of images A, B, and C, but also the faintness of image D. Dobler & Keeton (2005) were able, though, to find an acceptable model under the hypothesis that only image A is perturbed by small-scale structure. We conclude that the nature of the anomaly in B1422+231 is not yet clear, and generic magnification relations are not adequate for understanding this system.

6.5. *Cross Lenses*

The image pairs in cross lenses are not close pairs, but for completeness we still consider them in the context of the fold relation. Figure 11 compares the observed and predicted $R_{\rm fold}$ values for the six known cross lenses. The predicted distributions are all broad and centered at some positive value of $R_{\rm fold}$ (also see Fig. 5 and § 5.2). There are several cases of disagreement, which can be understood as follows. First, in Q2237+0305 microlensing perturbs the flux ratios, and in fact causes them to change with time (Woźniak et al. 2000).

Next, in HE 0435−1223, HST 14113+5211, and HST 12531−2914, several of the observed $R_{\rm fold}$ values lie to the left of the predicted distributions. However, our ellipsoid+shear lens models fit the flux ratios fairly well, provided that the shear is allowed to be moderately large ($\gamma = 0.13$ for HE 0435−1223, and $\gamma \sim 0.3$ for the other two). Such large shears are rare in the distribution used for our Monte Carlo simulations, which is why the predicted $R_{\rm fold}$ distributions in Figure 11 do not extend down to the observed values. They are not unreasonable, though, for lenses that lie in complex environments like groups or clusters,

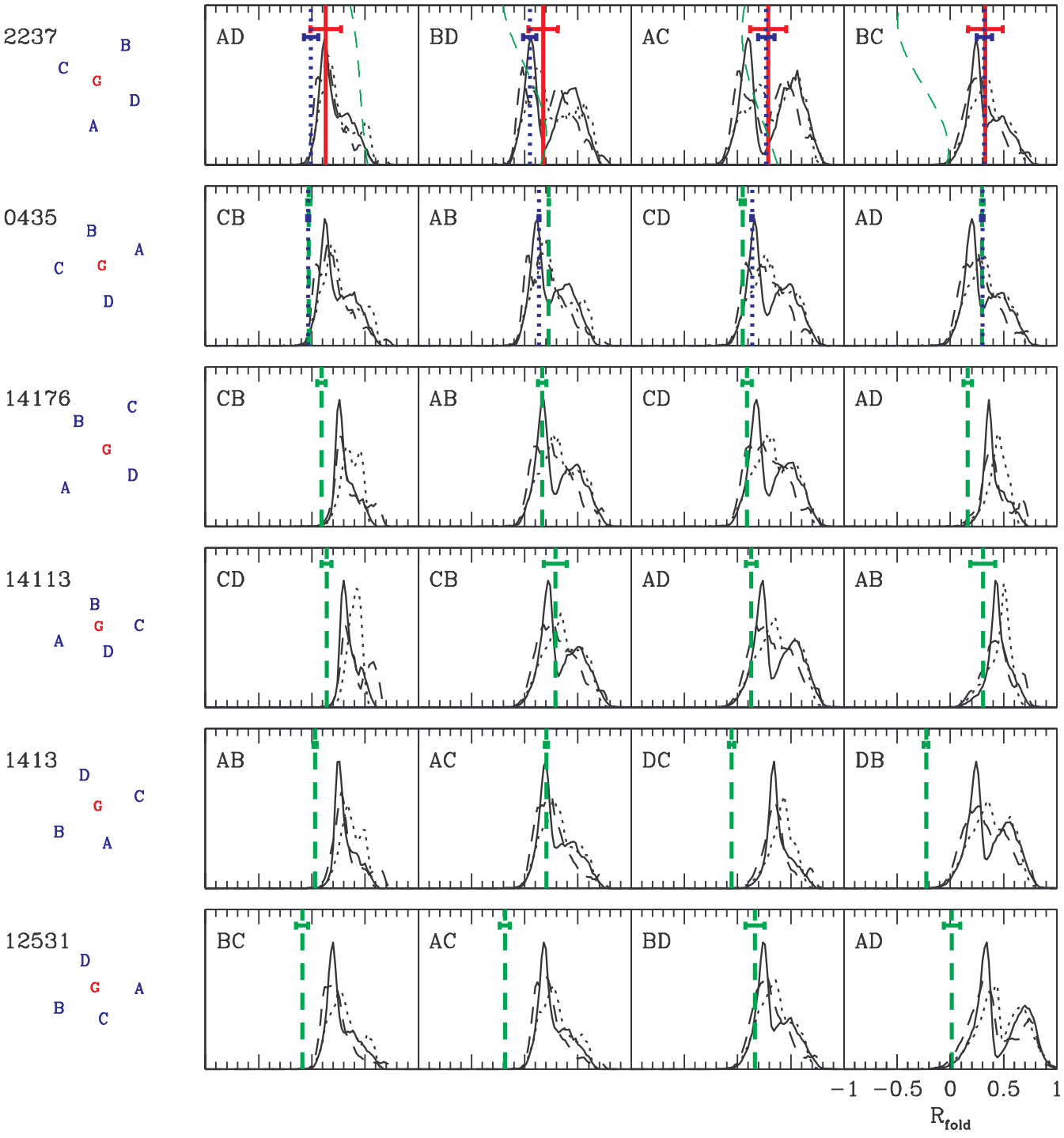

FIG. 11.—Similar to Fig. 7, but for the known cross lenses. For Q2237+0305, the vertical blue lines show mid-infrared values of $R_{\rm fold}$ (Agol et al. 2000); also, the green lines bend to represent the time variability in the optical flux ratios (Woźniak et al. 2000), with time running vertically. For HE 0435−1223, the vertical blue lines indicate data from optical emission-line flux ratios (Wisotzki et al. 2003).

which is probably the case for all three of these lenses (see Witt & Mao 1997; Fischer et al. 1998; Morgan et al. 2005). In other words, the discrepancies in Figure 11 for these three lenses indicate that there is "interesting" structure in the lens potential, but in this case it is probably structure in the environment of the lens as opposed to small-scale structure.

Finally, in HST 14176+5226 and HST 1413+117 there are discrepancies between the data and predictions that are not fully explained by a large shear. The fold relation cannot provide strong conclusions here, but it does suggest that these two systems deserve further study.

A striking general feature of Figure 11 is that nearly all the weight in the predicted probability distributions lies at $R_{\rm fold} > 0$, while some of the observed $R_{\rm fold}$ values are negative. We have argued that several of the negative observed values can be explained by large shears, which are absent from our Monte Carlo simulations. Thus, as a rule of thumb it appears that a negative $R_{\rm fold}$ value in a cross lens may indicate that

there is a significant environmental contribution to the lens potential.

7. CONCLUSIONS

When the source in a four-image gravitational lens system lies sufficiently close to a fold caustic, the two images that straddle the fold critical curve should be mirror images of each other, and the dimensionless flux combination $R_{\rm fold} \equiv (F_{\rm min} - F_{\rm sad})/(F_{\rm min} + F_{\rm sad})$ should vanish. A violation of this "fold relation" in an observed lens is thought to indicate that the lens galaxy has significant structure on scales smaller than the separation between the two close images. The fold relation may therefore join the cusp relation as an important model-independent method for identifying flux ratio anomalies that indicate small-scale structure.

We have learned, though, that the fold relation is more subtle and rich than was previously realized. The ideal fold relation $R_{\rm fold} \rightarrow 0$ holds only when the source is asymptotically close to a fold caustic. In more realistic situations, we find $R_{\rm fold} \propto u^{1/2} \propto d_1$, where u is the distance of the source from the caustic and d_1 is the distance between the two close images. In other words, $R_{\rm fold}$ goes to zero fairly slowly as the source approaches the caustic, which means that $R_{\rm fold} \neq 0$ might just indicate that the source sits a finite distance from the caustic. (For comparison, the cusp relation has a more rapid dependence $R_{\rm cusp} \propto d^2$; see Paper I.) If we seek to use the fold relation to identify flux ratio anomalies that indicate small-scale structure, then we must understand how much $R_{\rm fold}$ can deviate from zero just because of the finite offset of the source.

This is where we find our most startling result: $R_{\rm fold}$ is determined not just by the distance of the source from the caustic, but also by the location of the source *along* the caustic. If we write $R_{\rm fold} = A_{\rm fold} d_1 + \ldots$, then the coefficient $A_{\rm fold}$ varies enormously around the caustic. The problem is that the location of the source along the caustic, and hence the value of $A_{\rm fold}$, is not directly observable. Consequently, it is no simple matter to say how large $R_{\rm fold}$ must get before we can infer the presence of small-scale structure. Fortunately, the placement of the source along the caustic is encoded in the image configuration: not in the separation d_1 between the close pair of images, but rather in the distance d_2 to the next nearest image. (For example, a source near a fold but not near a cusp leads to $d_1 \ll d_2 \sim R_{\rm Ein}$, while a source near a cusp leads to $d_1 \sim d_2 \ll R_{\rm Ein}$.) We may still be able to predict the range of $R_{\rm fold}$ possible for a smooth lens potential, but only if we consider d_2 as well as d_1.

This general understanding allows us to develop a general method for using the fold relation to search for flux ratio anomalies in real lens systems. We postulate a reasonable and realistic population of smooth lens potentials containing ellipticity, octopole modes, and tidal shear, and use Monte Carlo simulations of four-image lenses produced by these lens potentials to derive the conditional probability distribution $p(R_{\rm fold}|d_1, d_2)$ for $R_{\rm fold}$ at fixed d_1 and d_2 (strictly speaking, fixed $d_1/R_{\rm Ein}$ and $d_2/R_{\rm Ein}$). We can then compare the observed value of $R_{\rm fold}$ for a real lens to the corresponding predicted distribution to determine whether the data are consistent with lensing by a smooth potential. In making our predictions, we actually consider three different galaxy populations in order to understand how our results depend on assumptions about what constitutes a "reasonable and realistic" lens population.

The fold relation applies most directly to the close pair of images in a lens with a fold configuration. Among the 12 known fold lenses, we find evidence for five violations: the optical (but not radio) fluxes in B0712+472; the optical fluxes in SDSS 0924+0219; the optical fluxes in PG 1115+080; the radio fluxes in B1555+375; and the radio fluxes in B1933+503. The optical anomalies in B0712+472 and SDSS 0924+0219 were already known from violations of the cusp relation (see Paper I), but it is valuable to see them identified by the fold relation as well. The optical anomaly in PG 1115+080 is not quite as secure as the others: the confidence level is 99.2% for two of our three sets of predictions, but only 96.1% for one that includes fairly strong octopole modes. Detailed lens modeling of PG 1115+080 suggests that multipole modes cannot provide an acceptable explanation of the flux ratio anomaly (Kochanek & Dalal 2004; Yoo et al. 2005), and while that conclusion is more model-dependent than ours, it does suggest that PG 1115+080 is indeed anomalous. The radio anomalies in B1555+375 and B1933+503 are newly revealed by the fold relation.

We believe that fold flux ratio anomalies provide robust and model-independent evidence for small-scale structure, for two reasons. First, the identification of the anomalies involves a *local* analysis of the lens mapping and thus relies only on local properties of the lens potential. This is precisely what we want in an analysis aimed at revealing small-scale, local structure. Second, we have explicitly shown that (apart from PG 1115+080) our conclusions do not change if we modify the parameter distributions that define our realistic galaxy population.

Based on our detailed analyses of individual fold lenses, we can extract a few rules of thumb. Since the sources in real lenses always lie a finite distance from a caustic, $R_{\rm fold}$ values in the range $0 \lesssim R_{\rm fold} \lesssim 0.2$ are predicted to be quite common and probably do *not* indicate flux ratio anomalies. When the separation between the two close images is small ($d_1/R_{\rm Ein} \lesssim 0.4$), the dependence on d_2 is not very strong; all that really matters is having d_2 be large enough for the image configuration to be identified as a fold. In this case, it appears that large values $R_{\rm fold} \gtrsim 0.2$ can reveal candidate anomalies. However, the fact that only one of four observed lenses with $R_{\rm fold} \approx 0.2$ is anomalous provides a strong reminder that a full and careful analysis of the fold relation must be done before drawing conclusions about anomalies. Finally, as d_1 increases, so too does the value of $R_{\rm fold}$ required to indicate an anomaly, and rules of thumb about the fold relation cease to be valid.

One final rule of thumb is that our smooth lens potentials almost always predict $R_{\rm fold} > 0$ for fold image pairs, indicating an asymmetry such that minimum images are generally expected to be brighter than saddle images in fold pairs. This point probably has implications for the prediction that substructure affects minima and saddles differently, tending to amplify minima but suppress saddles (Metcalf & Madau 2001; Schechter & Wambsganss 2002; Keeton 2003; Bradač et al. 2004), and for the observation that anomalous minima seem to be too bright while anomalous saddles seem to be too faint (Kochanek & Dalal 2004; Dobler & Keeton 2005). However, these issues are not yet fully understood, and further study is needed.

Our full analysis of the fold relation also allows us to apply it to the two close image pairs in a cusp lens. This application is more subtle because the analysis underlying the fold relation breaks down near a cusp caustic. Nevertheless, the predicted $R_{\rm fold}$ distribution for smooth lenses is bimodal with two narrow and well-separated peaks, which constitutes a sort of fold relation that can be used to evaluate observed $R_{\rm fold}$ values. We find that applying this fold relation to cusp lenses does not reveal any new anomalies beyond those that were identified by the cusp relation (Paper I). However, it may help us understand which of the three images is anomalous (a distinction that the cusp relation cannot make). For example, it appears that the strongest anomaly in RX J0911+0551 is probably in image A, while the strongest

anomaly in RX J1131−1231 is probably in image B. We take these conclusions less as definite statements and more as interesting suggestions to be examined with detailed lens models. One curious qualitative result is that, in cusp lenses, the fold relation appears to be more sensitive than the cusp relation to octopole modes. This fact limits our ability to find a clear violation of the fold relation in B2045+265, even though this lens has a very strong violation of the cusp relation.

Finally, we can also use our full understanding to apply the fold relation to all minimum/saddle pairs in all four images lenses, regardless of how close the pairs are. We must be very careful to remember that when $d_1 \gtrsim R_{\rm Ein}$ we are no longer performing a *local* analysis of the lens mapping, so we cannot claim to draw any model-independent conclusions about small-scale structure. Nevertheless, it is still interesting to determine which lenses seem to be inconsistent with lensing by an isothermal ellipsoid perturbed by octopole modes and moderate shear. Among fold lenses that do not have fold anomalies, we find that B0128+437, HE 0230−2130, SDSS 1004+4112, and WFI 2033−4723 all have discrepancies between the data and predictions for other image pairs.[17] In three of these cases (SDSS 1004+4112, HE 0230−2130, and WFI 2033−4723), the discrepancies are (presumably) caused by complex structure in the environment of the main lens galaxy. Finally, each of the six known cross lenses has at least one discrepant image pair. In Q2237+0305 the discrepancy is caused by microlensing. In three others (HST 12531−2914, HST 14113+5211, and H1413+117) it may be attributed to a large shear from a complex lens environment. Again, we emphasize that discrepancies in the fold relation for large-separation image pairs cannot be taken as strong evidence for small-scale structure. However, they can suggest that the lens potential has some interesting and complex structure that deserves further study.

At this point it is worthwhile to review the lenses in which violations the cusp and fold relations provide model-independent evidence for small-scale structure in the lens potential:

1. Among four known cusp lenses, there are three anomalies: RX J0911+0551 (optical), RX J1131−1231 (optical), and B2045+265 (radio).
2. Among 12 known fold lenses, there are five anomalies: B0712+472 (optical but not radio), SDSS 0924+0219 (optical), PG 1115+080 (optical), B1555+375 (radio), and B1933+503 (radio).

There may be other anomalies that are not identified by a generic analysis, but that are revealed by detailed lens modeling; B1422+231 is a prime example (Mao & Schneider 1998; Bradač et al. 2002; Metcalf & Zhao 2002; Dobler & Keeton 2005). Moreover, there may be systems among the "discrepant" lenses mentioned above that in fact contain small-scale structure; a good example is Q2237+0305, whose time-variable discrepancies are caused by microlensing (Woźniak et al. 2000). In other words, our accounting represents a strict *lower* bound on the number of lenses with flux ratio anomalies caused by small-scale structure—and makes it eminently clear that such anomalies are quite common.

Interpreting these anomalies to place constraints on the nature of the implied small-scale structure involves many considerations that are beyond the scope of this paper. No analysis of single-epoch, single-band photometry can determine the scale of the structure required to explain flux ratio anomalies, beyond the idea that it must be smaller than the separation between the images. Time variability (as in Q2237+0305) or differences between optical and radio flux ratios (as in B0712+472) may indicate microlensing, although even then a much more detailed analysis is required to determine the microlensing scale (e.g., Kochanek 2004 and references therein). Absent such data, it is impossible for any analysis of broadband photometry in individual lenses to robustly distinguish between microlensing, millilensing, or intermediate-scale phenomenon. All three possibilities are interesting, but they have very different implications for astrophysics.

Fortunately, there are excellent prospects for obtaining additional data that can help distinguish between the different hypotheses. Even apart from time variability, comparisons between optical continuum and broadband flux ratios can establish the scale of the small-scale structure (Moustakas & Metcalf 2003; Wisotzki et al. 2003; Metcalf et al. 2004; Morgan et al. 2004; Wayth et al. 2005a; Keeton et al. 2005). Showing that minimum and saddle images are affected differently by small-scale structure might also establish the scale (Metcalf & Madau 2001; Schechter & Wambsganss 2002; Keeton 2003; Kochanek & Dalal 2004; Bradač et al. 2004). These are several examples of the more general point that the size of the source quasar provides a scale in the problem that may help us determine the scale of structure in the lens (Dobler & Keeton 2005). It is important to note that all of these approaches require significant effort to obtain, analyze, and interpret new data; studying *all* four-image lenses in this much detail is not feasible. It is therefore crucial to have a reliable way to identify lenses that warrant further study. The fold relation joins the cusp relation in providing precisely the realistic but robust method that we need for identifying flux ratio anomalies. As such, the two relations provide the foundation for studies of small-scale structure in lens galaxies.

We thank Art Congdon and Greg Dobler for helpful discussions, and the anonymous referee for insightful comments. B. S. G. was supported by a Menzel Fellowship from the Harvard College Observatory. A. O. P. was supported by NSF grants DMS-0302812, AST 04-34277, and AST 04-33809, and an MIT Martin Luther King, Jr., Visiting Professorship in Physics.

[17] Actually, the discrepancy in HE 0230−2130 is seen in the fold pair, but it can be attributed to the presence of a second lens galaxy, so we prefer to discuss it here rather than among the fold flux ratio anomalies.

APPENDIX A

UNIVERSAL RELATIONS FOR FOLDS

The generic properties of lensing near a fold caustic have been studied before by Blandford & Narayan (1986), Schneider et al. (1992, see chap. 6), Petters et al. (2001, see chap. 9), and Gaudi & Petters (2002a). In this appendix we extend the analysis to a higher order of approximation.

A1. LOCAL ORTHOGONAL COORDINATES

Consider the lens equation $\boldsymbol{y} = \boldsymbol{x} - \mathrm{grad}\psi(\boldsymbol{x})$. If we assume that the induced lensing map, $\boldsymbol{\eta}(\boldsymbol{x}) = \boldsymbol{x} - \mathrm{grad}\psi(\boldsymbol{x})$, from the lens plane to the source plane is locally stable, then the caustics of $\boldsymbol{\eta}$ must be either folds or cusps (Petters et al. 2001, p. 294). Let us focus on a fold caustic, and translate coordinates in the lens and source planes so that the caustic passes through the origin $\boldsymbol{y} = \boldsymbol{0}$ of the light source plane, while the origin $\boldsymbol{x} = \boldsymbol{0}$ of the lens plane maps into the origin of the light source plane. By abuse of notation, we still use $\boldsymbol{x}$ and $\boldsymbol{y}$ to denote the translated coordinates.

Consider a small neighborhood N_L about the origin in the lens plane, which maps to a local region N_S about the origin in the source plane. We assume that N_S is sufficiently small that no critical points outside N_L are mapped into N_S, and there are no cusp caustic points inside N_S. In other words, the only caustic in N_S is a fold arc passing through the origin.

By Taylor-expanding, we see that the Jacobian matrix of the lensing map $\boldsymbol{\eta}$ is given at the origin $\boldsymbol{x} = \boldsymbol{0}$ by

$$[\mathrm{Jac}\,\boldsymbol{\eta}](\boldsymbol{0}) = \begin{bmatrix} 1 - 2\hat{a} & -\hat{b} \\ -\hat{b} & 1 - 2\hat{c} \end{bmatrix}, \tag{A1}$$

where

$$\hat{a} = \frac{1}{2}\psi_{11}(\boldsymbol{0}), \qquad \hat{b} = \psi_{12}(\boldsymbol{0}), \qquad \hat{c} = \frac{1}{2}\psi_{22}(\boldsymbol{0}). \tag{A2}$$

The subscripts indicate partial derivatives of ψ relative to $\boldsymbol{x} = (x_1, x_2)$. Note that ψ has no linear part (since $\boldsymbol{\eta}$ maps the origin to itself). For $\boldsymbol{y} = \boldsymbol{0}$ to be fold caustic point, the rank of $[\mathrm{Jac}\,\boldsymbol{\eta}](\boldsymbol{0})$ must be unity, which means that we must have $(1 - 2\hat{a})(1 - 2\hat{c}) - \hat{b}^2 = 0$ while at least one of $(1 - 2\hat{a})$, $(1 - 2\hat{c})$, and $\hat{b}^2$ does not vanish (Petters et al. 2001, p. 349). Consequently, $(1 - 2\hat{a})$ and $(1 - 2\hat{c})$ cannot both vanish. We lose no generality by assuming $1 - 2\hat{a} \neq 0$.

Now introduce the orthogonal matrix (see Petters et al. 2001, p. 344)

$$\boldsymbol{M} = \frac{1}{\sqrt{(1 - 2\hat{a})^2 + \hat{b}^2}} \begin{bmatrix} 1 - 2\hat{a} & -\hat{b} \\ \hat{b} & 1 - 2\hat{a} \end{bmatrix}, \tag{A3}$$

and define new orthogonal coordinates in the neighborhoods N_L and N_S by

$$\boldsymbol{\theta} = (\theta_1, \theta_2) \equiv \boldsymbol{M}\boldsymbol{x}, \qquad \boldsymbol{u} = (u_1, u_2) \equiv \boldsymbol{M}\boldsymbol{y}. \tag{A4}$$

(Note that the coordinate changes are the *same* in the lens and source planes, which is different from the approach of Schneider et al. 1992, p. 185.) Using these coordinates, Petters et al. (2001, p. 346) showed rigorously that $\boldsymbol{x} = \boldsymbol{0}$ is a fold critical point if and only if the following conditions hold:

$$(1 - 2\hat{a})(1 - 2\hat{c}) = \hat{b}^2, \qquad 1 - 2\hat{a} \neq 0, \qquad \hat{d} \equiv -\psi_{222}(\boldsymbol{0}) \neq 0. \tag{A5}$$

Remark.—The matrix $\boldsymbol{M}$ orthogonally diagonalizes $[\mathrm{Jac}\,\boldsymbol{\eta}](\boldsymbol{0})$.

Let us now Taylor expand the lens potential near the origin. We argue below that carrying the expansion to fourth order in $\boldsymbol{\theta}$ is both necessary and sufficient for the precision we desire. The most general fourth-order expansion can be written as (see Petters et al. 2001, pp. 346–347)

$$\psi(\boldsymbol{\theta}) = \frac{1}{2}(1 - \boldsymbol{K})\theta_1^2 + \frac{1}{2}\theta_2^2 + e\theta_1^3 + f\theta_1^2\theta_2 + g\theta_1\theta_2^2 + h\theta_2^3 + k\theta_1^4 + m\theta_1^3\theta_2 + n\theta_1^2\theta_2^2 + p\theta_1\theta_2^3 + r\theta_2^4. \tag{A6}$$

The zeroth-order term in the potential is irrelevant, so we neglect it. The first-order terms must vanish in order to ensure that the origin of the lens plane maps to the origin of the source plane. In the second-order terms, the coefficients of the $\theta_1\theta_2$ and θ_2^2 terms are fixed (to 0 and $\frac{1}{2}$, respectively) by the conditions that the origin is a fold critical point such that $[\mathrm{Jac}\,\boldsymbol{\eta}](\boldsymbol{0})$ is in diagonal form. Note that the coefficient e of the θ_1^3 term here is different from the ellipticity parameter used in the main text. We retain e here to match the notation used by Petters et al. (2001). The e coefficient does not appear in the main text, and the ellipticity parameter does not appear explicitly in this appendix, so there should be little confusion.

Conventional analyses of lensing near a fold caustic have only considered the K, e, f, g, and h terms in the expansion (Blandford & Narayan 1986; Schneider et al. 1992; Petters et al. 2001; Gaudi & Petters 2002a). However, we show below that some of the other terms are significant for our analysis.

A2. IMAGE POSITIONS AND MAGNIFICATIONS

We seek to use perturbation theory (e.g., Bellman 1966) to find expansions for the image positions and magnifications that are accurate to first order in $\boldsymbol{u}$. We work from our fourth-order expansion of the lens potential, and then verify that it is adequate for our

purposes. For bookkeeping purposes, let us introduce a scalar parameter ξ by taking $\boldsymbol{u} \rightarrow \xi \boldsymbol{u}$, so we can identify terms of a given order by examining the power of ξ.

For the potential equation (A6), the lens equation is

$$\xi u_1 = K\theta_1 - \left(3e\theta_1^2 + 2f\theta_1\theta_2 + g\theta_2^2\right) - \left(4k\theta_1^3 + 3m\theta_1^2\theta_2 + 2n\theta_1\theta_2^2 + p\theta_2^3\right), \tag{A7}$$

$$\xi u_2 = -\left(f\theta_1^2 + 2g\theta_1\theta_2 + 3h\theta_2^2\right) - \left(m\theta_1^3 + 2n\theta_1^2\theta_2 + 3p\theta_1\theta_2^2 + 4r\theta_2^3\right). \tag{A8}$$

Since the lowest order terms are linear or quadratic in $\boldsymbol{\theta}$, it is natural to postulate that the image positions can be written as a series expansion in ξ with the following form:

$$\theta_1 = \alpha_1\xi^{1/2} + \beta_1\xi + \mathcal{O}(\xi)^{3/2}, \tag{A9}$$

$$\theta_2 = \alpha_2\xi^{1/2} + \beta_2\xi + \mathcal{O}(\xi)^{3/2}. \tag{A10}$$

Substituting into the lens equation, we obtain

$$0 = (\alpha_1 K)\xi^{1/2} - (3\alpha_1^2 e + 2\alpha_1\alpha_2 f + \alpha_2^2 g - \beta_1 K + u_1)\xi + \mathcal{O}(\xi)^{3/2}, \tag{A11}$$

$$0 = -(\alpha_1^2 f + 2\alpha_1\alpha_2 g + 3\alpha_2^2 h + u_2)\xi - \left[2\alpha_1\beta_1 f + 2(\alpha_1\beta_2 + \alpha_2\beta_1)g + 6\alpha_2\beta_2 h + \alpha_1^3 m + 2\alpha_1^2\alpha_2 n + 3\alpha_1\alpha_2^2 p + 4\alpha_2^3 r\right]\xi^{3/2} + \mathcal{O}(\xi)^2. \tag{A12}$$

It is easily understood why these equations are carried to different orders. Equation (A7) has a term that is linear in $\boldsymbol{\theta}$, which means that correction terms appear at $\mathcal{O}(\xi)^{3/2}$. By contrast, in equation (A8) the lowest order term is quadratic in $\boldsymbol{\theta}$, and since

$$\theta_i\theta_j = \alpha_i\alpha_j\xi + (\alpha_i\beta_j + \alpha_j\beta_i)\xi^{3/2} + \mathcal{O}(\xi)^2, \tag{A13}$$

we see that the correction terms only appear at $\mathcal{O}(\xi)^2$.

Following perturbation theory, we can now solve for the unknowns α_i and β_i by demanding that equations (A11) and (A12) be satisfied at each order in ξ. We then find that the positions of the two images can be written as

$$\theta_1^{\pm} = \frac{3hu_1 - gu_2}{3hK}\xi + \mathcal{O}(\xi)^{3/2}, \tag{A14}$$

$$\theta_2^{\pm} = \mp\sqrt{\frac{-u_2}{3h}}\xi^{1/2} - \frac{3ghu_1 - (g^2 + 2Kr)u_2}{9h^2K}\xi + \mathcal{O}(\xi)^{3/2}. \tag{A15}$$

Note that the distance between the two images is

$$d_1 = 2\sqrt{\frac{-u_2}{3h}}\xi^{1/2} + \mathcal{O}(\xi)^{3/2}. \tag{A16}$$

To find the magnifications of the images, we compute the Jacobian determinant of the lens equation and evaluate that at $\boldsymbol{\theta}^{\pm}$ to obtain

$$\left(\mu^{\pm}\right)^{-1} = \pm 2K\sqrt{-3hu_2}\xi^{1/2} + \frac{4}{3h}\left(g^2 - 3fh + 2Kr\right)u_2\xi + \mathcal{O}(\xi)^{3/2}. \tag{A17}$$

This result shows that the $\pm$ labels for the two images have been assigned such that $\mu^+ > 0$ while $\mu^- < 0$.

Remarks.—(1) To check our results, we note that at lowest order we recover the same scalings $d_1 \propto \xi^{1/2}$ and $\mu^{\pm} \propto \xi^{-1/2}$ found by previous analyses (Schneider et al. 1992; Petters et al. 2001; Gaudi & Petters 2002a). (2) To first order in ξ the image separation and the two magnifications depend only on the u_2 component of the source position. (3) In several places we have $(-hu_2)^{1/2}$ or $(-u_2/h)^{1/2}$. In general, at least for simple lens potentials like an isothermal ellipsoid or isothermal sphere with shear, we have $h \leq 0$ all along the caustic. This means that only source positions with $u_2 > 0$ lead to the production of two fold images.

At first order in the image positions and magnifications, the presence of r demonstrates that the fourth-order terms in equation (A6) cannot be ignored. At the same time, we can now verify that going to fourth order is sufficient. Any term of $\mathcal{O}(\boldsymbol{\theta})^5$ in the potential would enter the lens equation at $\mathcal{O}(\boldsymbol{\theta})^4$; that would in turn be of order ξ^2 or higher, which is beyond the order to which we are working. Similarly, terms of $\mathcal{O}(\boldsymbol{\theta})^5$ in the potential would enter μ^{-1} at $\mathcal{O}(\boldsymbol{\theta})^3$ or at least $\xi^{3/2}$. In other words, going to fourth order in equation (A6) is both necessary and sufficient when we seek the image positions and magnifications correct to first order in ξ.

A3. GENERIC BEHAVIOR OF THE FOLD RELATION

From equation (A17) we see that the two fold images have magnifications that are equal and opposite to lowest order in ξ, which means that the combination $|\mu^+| - |\mu^-|$ should approximately vanish. In observed lenses, the magnifications are not directly observable but the fluxes are, so to construct a dimensionless combination of the fluxes we define

$$R_{\rm fold} \equiv \frac{|\mu^+| - |\mu^-|}{|\mu^+| + |\mu^-|} = \frac{F^+ - F^-}{F^+ + F^-}. \tag{A18}$$

Plugging in the series expansions for $\mu^{\pm}$, we find

$$R_{\rm fold} = \frac{2(g^2 - 3fh + 2Kr)}{3hK}\sqrt{\frac{-u_2}{3h}}\xi^{1/2} + \mathcal{O}(\xi). \tag{A19}$$

By comparing the expansion for d_1 in equation (A16), we see that we can write

$$R_{\rm fold} = A_{\rm fold} d_1 + \mathcal{O}(\xi), \tag{A20}$$

where

$$A_{\rm fold} \equiv \frac{g^2 - 3fh + 2Kr}{3hK} = \frac{3\psi_{122}^2 - 3\psi_{112}\psi_{222} + \psi_{2222}(1 - \psi_{11})}{6\psi_{222}(1 - \psi_{11})}. \tag{A21}$$

In the last equality, we have replaced the coefficients (f, g, h, K, r) with their definitions in terms of derivatives of the potential; for example,

$$f = \frac{1}{2}\psi_{112} = \frac{1}{2}\frac{\partial^3\psi}{\partial\theta_1^2\partial\theta_2}, \qquad g = \frac{1}{2}\psi_{122} = \frac{1}{2}\frac{\partial^3\psi}{\partial\theta_1\partial\theta_2^2}, \tag{A22}$$

and so forth, where the derivatives are evaluated at the origin $\boldsymbol{\theta} = \mathbf{0}$.

To summarize, $R_{\rm fold}$ vanishes for a source asymptotically close to a fold caustic. For a source a small but finite distance away, there is a correction term that scales as the square root of the distance of the source from the caustic, or (more usefully) as the separation between the two fold images. The coefficient $A_{\rm fold}$ of this linear scaling depends on properties of the lens potential at the fold critical point. In particular, the presence of r reiterates the fact that the fourth-order expansion in the potential (eq. [A6]) is necessary to obtain an expansion for $R_{\rm fold}$ that is accurate at order $\xi^{1/2}$ or d_1.

We have verified all of the approximations in this appendix by comparing them to exact numerical solutions of the lens equation obtained with the software by Keeton (2001).

APPENDIX B

DATA FOR THE OBSERVED FOUR-IMAGE LENSES

In this appendix we summarize the observational data that we use for all of the observed four-image lenses; this text complements the data values given in Table 1. For each lens system, we need the relative positions of the lensed images in order to measure the separations d_1 and d_2, and also to use as constraints on lens models for determining the Einstein radius $R_{\rm Ein}$. The position of the lens galaxy (or galaxies), if available, is also valuable for the lens modeling. We also need the flux ratios between the images in order to determine $R_{\rm fold}$. We consider radio and optical/near-infrared flux ratios separately, because they are believed to correspond to very different source sizes and provide very different information about small-scale structure in the lens potential (see, e.g., Dalal & Kochanek 2002; Dobler & Keeton 2005). At optical/near-infrared wavelengths, we examine the colors of the images to detect (and correct for) any differential extinction that may be present. Falco et al. (1999) carried out a detailed version of this analysis for a sample of lenses that includes seven that we consider, and we use their results where available. If there is no evidence for differential extinction, we combine data from different passbands using a weighted average. At radio wavelengths, we again examine the wavelength dependence of the flux ratios to determine that there are no significant electromagnetic effects. If there are other flux measurements, such as in optical broad emission lines or at mid-infrared wavelengths, we use those as well (as discussed below).

0047−2808.—This is a quadruply imaged system (Warren et al. 1996, 1999), but its lack of pointlike images means that it requires special modeling techniques (e.g., Wayth et al. 2005b) and that it is probably not very interesting for the analysis of small-scale structure anyway. We do not include it in our sample.

B0128+437.—For the image positions, we use the radio astrometry from Phillips et al. (2000). For the radio fluxes, we use the mean and scatter in $R_{\rm fold}$ from 41 epochs of MERLIN monitoring by Koopmans et al. (2003a). The monitoring shows no evidence for time dependence.

HE 0230−2130.—We use the optical *Hubble Space Telescope* (*HST*) astrometry from CASTLES (CfA-Arizona Space Telescope Lens Survey).[18] There are two lens galaxies; we include both of them in lens models, taking their observed positions as constraints but optimizing their masses. For the optical fluxes of the lensed images, we use the *BRI* data for images A, B, and C from Wisotzki et al. (1999). The colors are consistent with no differential extinction. (Image D is not well separated from galaxy G2 in the Wisotzki et al. data, so we do not consider it.)

MG 0414+0534.—We use the optical *HST* astrometry from CASTLES. We include the satellite galaxy near the lens galaxy ("object X"; Schechter & Moore 1993) in lens models. For the optical image fluxes, we use the extinction-corrected flux ratios from Falco et al. (1999). For the radio fluxes, we use the high-resolution VLBI data from Trotter et al. (2000). Those observations resolve each image into four subcomponents; the $R_{\rm fold}$ values are similar for the different subcomponents, so we take the weighted average. The radio flux ratios are constant in time to 1%–3% (Moore & Hewitt 1997).

HE 0435−1223.—We use the optical *HST* astrometry from CASTLES. For the optical broadband fluxes, we use the *gri* data from Wisotzki et al. (2002). Wisotzki et al. (2003) also report emission-line fluxes; we take the mean and scatter in $R_{\rm fold}$ from the C IV and C III] lines. There is no evidence for wavelength dependence in the broadband flux ratios, and the spectra of the different images have identical spectral slopes, so there does not appear to be any differential extinction. Image D appeared to vary by 0.07 mag between the two sets of observations, which may imply evidence for microlensing.

B0712+472.—We use the optical *HST* astrometry and photometry from CASTLES. The values of $R_{\rm fold}$ differ slightly in the *V*, *I*, and *H* bands, but within the measurement uncertainties; hence there is no evidence for differential extinction. For the radio fluxes, we use the mean and scatter in $R_{\rm fold}$ from MERLIN monitoring by Koopmans et al. (2003a). There is evidence for time dependence in the radio fluxes.

RX J0911+0551.—We use the optical *HST* astrometry and photometry from CASTLES. The lens galaxy has a satellite galaxy, which we include in lens models. The image flux ratios vary with wavelength in a manner that is consistent with differential extinction, so we correct for extinction using a redshifted $R_V = 3.1$ extinction curve from Cardelli et al. (1989; see also Paper I).

SDSS 0924+0219.—Keeton et al. (2005) report image positions, broadband flux ratios, and broad emission line flux ratios from *HST* observations. We use the weighted average of the *V* and *I* broadband flux ratios. We use the emission-line fluxes with 5% uncertainties, which is probably conservative. The best color information comes from *gri* data by Inada et al. (2003), which are consistent with no differential extinction.

SDSS 1004+4112.—This lens is produced by a cluster rather than a single galaxy (Oguri et al. 2004), but we can still treat it with our formalism. We use ground-based *griz* data from Oguri et al. (2004), and *HST*/*I* data from Inada et al. (2005). There is no evidence for differential extinction. Richards et al. (2004) claimed to observe microlensing of the broad emission lines in image A, but the level of variability in the continuum is not yet known.

PG 1115+080.—We use the *HST* astrometry and photometry from CASTLES, and the mid-infrared flux ratios from Chiba et al. (2005). Falco et al. (1999) find that the *VIH* data are consistent with no differential extinction. In the lens models, we explicitly include the group of galaxies surrounding the lens (see Keeton & Kochanek 1997; Impey et al. 1998).

RX J1131−1231.—We use the ground-based astrometry and photometry from Sluse et al. (2003). They report two epochs of *V* data and one epoch of *R*. The colors are consistent with no differential extinction. The total flux varied between the two epochs, but the flux ratios remained constant.

HST 12531−2914.—We use the *HST* astrometry and photometry from Ratnatunga et al. (1995) and CASTLES. Falco et al. (1999) find that the $V - I$ colors are consistent with no extinction (within the noise).

HST 14113+5211.—We use the *HST* astrometry and photometry from Fischer et al. (1998) and CASTLES. There is some scatter among the values of $R_{\rm fold}$ obtained from *V*-, *R*-, and *I*-band data, but the scatter is within the (fairly large) measurement uncertainties.

H1413+117.—We use the *HST* astrometry from CASTLES. For the optical fluxes, we use the extinction-corrected flux ratios from Falco et al. (1999).

HST 14176+5226.—We use the *HST* astrometry and photometry from Ratnatunga et al. (1995). Falco et al. (1999) find that the colors are consistent with no differential extinction.

B1422+231.—We use the radio data from Patnaik et al. (1999). The radio fluxes are basically constant in time (Patnaik & Narasimha 2001). For the optical fluxes, we use the extinction-corrected flux ratios from Falco et al. (1999). We also use the mid-infrared flux ratios between images A, B, and C (image D was not detected) from Chiba et al. (2005).

B1555+375.—We use the radio data from Marlow et al. (1999). The data from radio monitoring by Koopmans et al. (2003a) yield similar results, but have larger formal errors.

B1608+656.—Fassnacht et al. (2002) monitored the radio fluxes, measured the time delays, and determined the delay-corrected magnification ratios; we take the mean and scatter in $R_{\rm fold}$ from their three seasons of data. There are two lens galaxies; we model the system using data from Koopmans et al. (2003b).

B1933+503.—There are ten lensed images associated with three different sources. We use all of the images in lens modeling, following Cohn et al. (2001). However, for the fold analysis we use only the fold quad consisting of images 1/3/4/6. For the radio fluxes, we first take the mean and scatter from 8.4 GHz monitoring by Biggs et al. (2000), and then combine that in weighted average with measurements at other wavelengths by Sykes et al. (1998).

WFI 2026−4536.—We use the optical data from Morgan et al. (2004). We use all available data in which the images are resolved: *ugriHK*$_s$ plus *HST* F160W for images B and C; and *iHK*$_s$ plus *HST* F160W for images A_1 and A_2. There is some wavelength

[18] See http://cfa-www.harvard.edu/castles.

dependence that may suggest differential extinction or microlensing; the current data are inconclusive. We simply take the mean and scatter in $R_{\rm fold}$ from all of the data.

WFI 2033−4723.—We use the optical data from Morgan et al. (2004). For the optical broadband flux ratios, we use all available data in which the images are resolved: *ugri* for images B and C; and *ri* for images A_1 and A_2. Morgan et al. also report emission-line flux ratios; we take the weighted average of $R_{\rm fold}$ from the C IV, C III], and Mg II lines.

B2045+265.—We use the radio positions from Fassnacht et al. (1999). For the radio fluxes, we combine various measurements by Fassnacht et al. (1999) and monitoring by Koopmans et al. (2003a), and take the mean and scatter in $R_{\rm fold}$. For the optical fluxes, we use *HST* data from CASTLES for images A, B, and C (image D was not detected). The *VIH* colors are consistent with no differential extinction.

Q2237+0305.—We use *HST* astrometry from CASTLES. For the broadband optical fluxes, we use the microlensing light curves from Woźniak et al. (2000). We correct for differential extinction using the reddening deduced by Falco et al. (1999). For the radio fluxes, we use the data from Falco et al. (1996). In addition, Agol et al. (2000) report mid-infrared flux ratios measured at 8.9 and 11.7 μm.

REFERENCES

Agol, E., Jones, B., & Blaes, O. 2000, ApJ, 545, 657
Amara, A., Metcalf, R. B., Cox, T. J., & Ostriker, J. P. 2004, preprint (astro-ph/0411587)
Bellman, R. 1966, Perturbation Techniques in Mathematics, Engineering, and Physics (Dover: Mineola)
Bender, R., Surma, P., Döbereiner, S., Möllenhoff, C., & Madejski, R. 1989, A&A, 217, 35
Bernstein, G., Fischer, P., Tyson, J. A., & Rhee, G. 1997, ApJ, 483, L79
Biggs, A. D., Xanthoupoulos, E., Browne, I. W. A., Koopmans, L. V. E., & Fassnacht, C. D. 2000, MNRAS, 318, 73
Blandford, R., & Narayan, R. 1986, ApJ, 310, 568
Bradač, M., Schneider, P., Lombardi, M., Steinmetz, M., Koopmans, L. V. E., & Navarro, J. F. 2004, A&A, 423, 797
Bradač, M., Schneider, P., Steinmetz, M., Lombardi, M., King, L. J., & Porcas, R. 2002, A&A, 388, 373
Cardelli, J. A., Clayton, G. C., & Mathis, J. S. 1989, ApJ, 345, 245
Chen, J., Kravtsov, A. V., & Keeton, C. R. 2003, ApJ, 592, 24
Chiba, M. 2002, ApJ, 565, 17
Chiba, M., Minezaki, T., Kashikawa, N., Kataza, H., & Inoue, K. T. 2005, ApJ, 627, 53
Cohn, J. D., Kochanek, C. S., McLeod, B. A., & Keeton, C. R. 2001, ApJ, 554, 1216
Congdon, A., & Keeton, C. R. 2005, MNRAS, in press (astroph/0510232)
Dalal, N. 1998, ApJ, 509, L13
Dalal, N., & Kochanek, C. S. 2002, ApJ, 572, 25
Dalal, N., & Watson, C. R. 2004, preprint (astro-ph/0409483)
Dobler, G., & Keeton, C. R. 2005, MNRAS, submitted (astro-ph/0502436)
Evans, N. W., & Hunter, C. 2002, ApJ, 575, 68
Evans, N. W., & Witt, H. J. 2003, MNRAS, 345, 1351
Falco, E. E., Lehár, J., Perley, R. A., Wambsganss, J., & Gorenstein, M. V. 1996, AJ, 112, 897
Falco, E. E., et al. 1999, ApJ, 523, 617
Fassnacht, C. D., Xanthopoulos, E., Koopmans, L. V. E., & Rusin, D. 2002, ApJ, 581, 823
Fassnacht, C. D., et al. 1999, AJ, 117, 658
Fischer, P., Schade, D., & Barrientos, L. P. 1998, ApJ, 503, L127
Gaudi, B. S., & Petters, A. O. 2002a, ApJ, 574, 970
———. 2002b, ApJ, 580, 468
Heyl, J. S., Hernquist, L., & Spergel, D. N. 1994, ApJ, 427, 165
Holder, G., & Schechter, P. 2003, ApJ, 589, 688
Hunter, C., & Evans, N. W. 2001, ApJ, 554, 1227
Impey, C. D., et al. 1998, ApJ, 509, 551
Inada, N., et al. 2003, AJ, 126, 666
———. 2005, PASJ, 57, L7
Jørgensen, I., Franx, M., & Kjærgaard, P. 1995, MNRAS, 273, 1097
Keeton, C. R. 2001, preprint (astro-ph/0102340)
———. 2003, ApJ, 584, 664
Keeton, C. R., Burles, S., Schechter, P. L., & Wambsganss, J. 2005, ApJL, submitted (astro-ph/0507521)
Keeton, C. R., Gaudi, B. S., & Petters, A. O. 2003, ApJ, 598, 138 (Paper I)
Keeton, C. R., & Kochanek, C. S. 1997, ApJ, 487, 42
Keeton, C. R., Kochanek, C. S., & Seljak, U. 1997, ApJ, 482, 604
Keeton, C. R., & Winn, J. N. 2003, ApJ, 590, 39
Keeton, C. R., et al. 2000, ApJ, 542, 74
Klypin, A., Kravtsov, A. V., Valenzuela, O., & Prada, F. 1999, ApJ, 522, 82
Kochanek, C. S. 1991, ApJ, 373, 354
———. 2004, 605, 58
Kochanek, C. S. 2005, in Proc. IAU Symp. 225, The Impact of Gravitational Lensing on Cosmology, ed. Y. Mellier & G. Meylan (Cambridge: Cambridge Univ. Press)
Kochanek, C. S., & Dalal, N. 2004, ApJ, 610, 69
Koopmans, L. V. E., et al. 2003a, ApJ, 595, 712
———. 2003b, ApJ, 599, 70
Mao, S. 1992, MNRAS, 389, 63
Mao, S., Jing, Y., Ostriker, J. P., & Weller, J. 2004, ApJ, 604, L5
Mao, S., & Schneider, P. 1998, MNRAS, 295, 587
Marlow, D. R., et al. 1999, AJ, 118, 654
Metcalf, R. B. 2005a, ApJ, 622, 72
———. 2005b, ApJ, 629, 673
Metcalf, R. B., & Madau, P.. 2001, ApJ, 563, 9
Metcalf, R. B., Moustakas, L. A., Bunker, A. J., & Parry, I. R. 2004, ApJ, 607, 43
Metcalf, R. B., & Zhao, H. 2002, ApJ, 567, L5
Moore, B., Ghigna, S., Governato, F., Lake, G., Quinn, T., Stadel, J., & Tozzi, P. 1999, ApJ, 524, L19
Moore, C. B., & Hewitt, J. N. 1997, ApJ, 491, 451
Morgan, N. D., Kochanek, C. S., Pevunova, O., & Schechter, P. L. 2005, AJ, 129, 2531
Morgan, N. D., et al. 2004, AJ, 127, 2617
Moustakas, L. A., & Metcalf, R. B. 2003, MNRAS, 339, 607
Naab, T., & Burkert, A. 2003, ApJ, 597, 893
Oguri, M., & Lee, J. 2004, MNRAS, 355, 120
Oguri, M., et al. 2004, ApJ, 605, 78
Patnaik, A. R., Kemball, A. J., Porcas, R. W., & Garrett, M. A. 1999, MNRAS, 307, L1
Patnaik, A. R., & Narasimha, D. 2001, MNRAS, 326, 1403
Petters, A. O., Levine, H., & Wambsganss, J. 2001, Singularity Theory and Gravitational Lensing (Boston: Birkhäuser)
Phillips, P. M., et al. 2000, MNRAS, 319, L7
Ratnatunga, K., Ostrander, E. J., Griffiths, R. E., & Im, M. 1995, ApJ, 453, L5
Rest, A., van den Bosch, F. C., Jaffe, W., Tran, H., Tsvetanov, Z., Ford, H. C., Davies, J., & Schafer, J. 2001, AJ, 121, 2431
Richards, G. T., et al. 2004, ApJ, 610, 679
Rusin, D., & Tegmark, M. 2001, ApJ, 553, 709
Rusin, D., et al. 2001, ApJ, 557, 594
Saglia, R. P., Bender, R., & Dressler, A. 1993, A&A, 279, 75
Saha, P., & Williams, L. L. R. 2003, AJ, 125, 2769
Schechter, P. L., & Moore, C. B. 1993, AJ, 105, 1
Schechter, P. L., & Wambsganss, J. 2002, ApJ, 580, 685
Schechter, P. L., et al. 2003, ApJ, 584, 657
Schneider, P., Ehlers, J., & Falco, E. E. 1992, Gravitational Lenses (Berlin: Springer)
Schneider, P., & Weiss, A. 1992, A&A, 260, 1
Sluse, D., et al. 2003, A&A, 406, L43
Sykes, C. M., et al. 1998, MNRAS, 301, 310
Trotter, C. S., Winn, J. N., & Hewitt, J. N. 2000, ApJ, 535, 671
Warren, S. J., Hewett, P. C., Lewis, G. F., Møller, P., Iovino, A., & Shaver, P. A. 1996, MNRAS, 278, 139
Warren, S. J., Lewis, G. F., Hewett, P. C., Møller, P., Shaver, P. A., & Iovino, A. 1999, A&A, 343, L35
Wayth, R. B., O'Dowd, M., & Webster, R. L. 2005a, MNRAS, 359, 561
Wayth, R. B., Warren, S. J., Lewis, G. F., & Hewett, P. C. 2005b, MNRAS, 360, 1333
Winn, J. N., Kochanek, C. S., Keeton, C. R., & Lovell, J. E. J. 2003, ApJ, 590, 26

Wisotzki, L., Becker, T., Christensen, L., Helms, A. Jahnke, K., Kelz, A., Roth, M. M., & Sanchez, S. F. 2003, A&A, 408, 455
Wisotzki, L., Christleib, N., Liu, M. C., Maza, J., Morgan, N. D., & Schechter, P. L. 1999, A&A, 348, L41
Wisotzki, L., Schechter, P. L., Bradt, H. V., Heinmüller, J., & Reimers, D. 2002, A&A, 395, 17
Witt, H. J., & Mao, S. 1997, MNRAS, 291, 211
———. 2000, MNRAS, 311, 689
Woźniak, P. R., Alard, C. Udalski, A., Szymański, M., Kubiak, M., Pietrzyński, G., & Zebruń, K. 2000, ApJ, 529, 88
Yoo, J., Kochanek, C. S., Falco, E. E., & McLeod, B. A. 2005, ApJ, 626, 51
Zentner, A. R., & Bullock, J. S. 2003, ApJ, 598, 49